Date paper revised: 2 June 2015

Thermo-poro-mechanical analysis of landslides: from creeping behaviour to catastrophic failure

E. E. Alonso [(1)], A. Zervos [(2)], N.M. Pinyol [(1,3)]

(1): Department of Geotechnical Engineering and Geosciences, UPC, Barcelona

(2): Faculty of Engineering and the Environment, University of Southampton

(3): International Center for Numerical Methods in Engineering

Corresponding Author: Eduardo E. Alonso

eduardo.alonso@upc.edu

ABSTRACT

Catastrophic landslides are characterized by high velocities (1 to 100 m/s), large displacements (tens to hundreds of meters) and, in most cases, by a large mobilized mass, in excess of 1Mm^3. The scope of the paper encompasses planar and compound sliding motions which may exhibit creeping behaviour during a certain period but may evolve to a very rapid motion. Thermo-mechanical interactions, at the scale of the sliding surface, are accepted as a critical aspect to explain these motion phases and their relationship.

The paper reviews the mechanisms leading to strength reduction of the failure surface and the published thermo-mechanical formulations. They share a common basic structure. The sliding kinetics and global equilibrium are described at a large scale (the landslide itself) and the evolving shearing strength at the sliding surface derives from the "local" analysis of the shearing band and its vicinity. Pore pressures, temperatures and related variables are estimated by resolving a set of balance equations. Both scales are fully coupled. A significant aspect analyzed in detail in the paper is the transition from creeping motions to a rapid event. It requires the joint consideration of strain-rate effects on friction and the thermo-poro-mechanical analysis of the shearing band and its vicinity. Results are found in terms of dimensionless numbers which control the entire phenomenon. Calculation of the slide evolution requires special numerical techniques described in the paper. Band permeability is found to be the dominant property controlling the triggering of fast motions. The creeping stage and the eventual slide blowup are intimately linked. This relationship is explored in the paper.

Although this is not pursued in this paper, the models presented can be readily used to back-analyse relevant case histories or, in principle, even to carry out predictive modelling, provided an adequate calibration is available for the material parameters.

KEYWORDS: landslides, shear strength, temperature effects, strain localization, creep, pore pressures.

Notation list

A: model parameter defining the effect of velocity on strength

a: model parameter defining the effect of strain rate on friction angle

c_s: specific heat of solid particles

c_w: specific heat of water

D: planar landslide thickness

E: energy barrier

e: thickness of the shear band

E_1: reference energy barrier

f^*: basic friction for $v=v^*$ and $\psi=0$

f_v: function defining the effect of sliding velocity on friction angle

g: gravitational acceleration

$\hat{H}$: dimensionless heat generated in the shear band

h_w: water height above the sliding plane

k: saturated permeability

L_{u_w} : z coordinate where a boundary condition for excess pore water pressure is applied

L_θ : z coordinate where a boundary condition for temperature is applied

$\hat{L}_\theta$: dimensionless L_θ

m_{soil}: compressibility coefficient of the soil skeleton

64 m_v: oedometric compressibility coefficient of soil

65 n: porosity

66 p_w: initial pore water pressure

67 $\hat{p}_w$: dimensionless initial pore water pressure

68 R: universal gas constant

69 SF: safety factor

70 T: absolute temperature

71 t: time

72 u_w: excess pore water pressure

73 $\hat{u}_w$: dimensionless excess pore water pressure

74 $\hat{u}_w^{\max}$: dimensionless maximum excess pore water pressure

75 v^*: velocity below which friction does not depend on velocity

76 v: sliding velocity

77 $\hat{v}$: dimensionless sliding velocity

78 v_1: reference shearing rate

79 v_{ref}: reference velocity

80 $\hat{v}_{ref}$: dimensionless reference velocity

81 z: vertical spatial coordinate

82 $\hat{z}$: dimensionless vertical spatial coordinate

α_w: compressibility coefficient of water

β: inclination of sliding surface

$\beta_{s:}$ thermal expansion coefficient of solid particles

$\beta_{soil:}$ thermal expansion coefficient of saturated porous media

$\beta_{w:}$ thermal expansion coefficient of water

$\dot{\delta}$: sliding velocity

$\dot{\varepsilon}$: strain rate

$\dot{\varepsilon}_0$: reference strain rate

ϕ'_0: reference frictional angle associated with a reference strain rate ($\dot{\varepsilon}_0$)

ϕ': effective friction angle

γ_w: water specific weight

Γ: Fourier's thermal conductivity of saturated porous media

Γ_s: Fourier's thermal conductivity of solid particles

Γ_w: Fourier's thermal conductivity of water

μ: friction coefficient

$\mu_{0:}$ reference friction coefficient

Θ: dimensionless coefficient associated with heat flow in the heat balance equation

θ: temperature

$\hat{\theta}$: dimensionless temperature

θ_0: reference temperature

Π: dimensionless coefficient associated with thermal expansion of porous rock in the mass balance equation of water

ρ: density of saturated porous media

ρ_s: density of solid particles

ρ_w: water density

$(\rho c)_s$: specific heat of saturated porous media

σ: normal stress to the sliding plane

σ_c: normal stress to the sliding plane acting at molecular scale

τ: shear stress along the sliding plane

τ_c: shear adhesion stress acting at molecular scale

Σ: dimensionless coefficient associated with stress induced volumetric deformation in the mass balance equation of water

ξ_0: reference value of ξ

ξ: state variable which accounts for strengthening and weakening effects on the friction coefficient

Ω: active volume of contact bonds

Ψ: dimensionless coefficient associated with the source term in the heat balance equation

$\bar{\Psi}$: variable to include other effects than those associated with shearing velocity on frictional strength

Thermo-poro-mechanical analysis of landslides: from creeping behaviour to catastrophic failure

E. E. Alonso, A. Zervos, N.M. Pinyol

1. INTRODUCTION

Large catastrophic landslides are a constant threat to human communities and infrastructure works. Their danger derives from the large volumes of rock mass they involve (well in excess of 1million m^3) and their high estimated sliding velocities (10m/s to 100m/s). Sosio et al (2008) list a number of historical rock avalanches and their main characteristics. The known number of catastrophic landslides is, however, much larger and there is a continuous arrival of new cases, triggered by different natural and anthropogenic causes: earthquakes, heavy rain, reservoir impounding and rapid drawdown and excavations or river erosion. A wider view of catastrophic landslides at a regional scale and its interaction with other geodynamic processes is given by Hewitt et al (2008). Active mountain formation and the associated ongoing crustal plate collisions indicate the natural occurrence of these events, which is not expected to decrease in time.

A classic landslide that has been extensively studied is that of Vaiont; Hendron and Patton (1985), Müller (1964), Nonveiller (1987), Semenza (2001) and Paronuzzi et al (2013) provide detailed and informative contributions. Other large scale catastrophic landslides associated with reservoir operations have been reported by Alcántara-Ayala and Domínguez-Morales (2008) (San Juan de Grijalva slide in Mexico, 2007); Wang et al (2004) and Dai et al (2004) (Qiangjianping slide in China, towards the reservoir of the Three Gorges Project, 2003); Chamot (1993), Plaza-Netos and Zevallos (1994), Schuster *et al.,* (2002) and Harden (2004) (La Josefina landslide, Ecuador, in 1993). An often reported case in recent years is the giant Tsaoling landslide, Taiwan, that was triggered by the 1999 Chi-Chi earthquake (Chen et al, 2003; Tang et al, 2009; Liao et al, 2011; Wu and Chen, 2011; Yang et al, 2014.) In general, the

149 interpretation of earthquake induced motion requires velocity- and, in some cases,
150 displacement-dependent shear strength weakening of the failure surface. This “slip
151 weakening” effect is discussed below because of its attributed relevance to the sudden
152 acceleration of rapid slides.

153 The morphology and dynamics of these events is quite diverse. Hungr et al (2014) provide an
154 updated classification of landslides but, for the purpose of this paper, we may broadly
155 distinguish flow-like motions from motions with a dominant sliding mode of deformation. This
156 distinction is relevant when considering the mathematical methods of analysis available. In the
157 first case hydrodynamic motion equations and soil/rock properties often associated with the
158 concept of viscosity have been developed (Iverson et al 1997; Cascini et al 2010; Pastor et al
159 2014). In the second case attention is concentrated on the position and frictional
160 characteristics of the sliding surfaces, which should satisfy conditions of kinematic
161 compatibility. This is the approach followed here. Further, a large number of numerical
162 modelling techniques exist, capable of simulating landslide initiation and motion. Methods for
163 the analysis of continua such as the FEM or the MPM (Duncan 1996; Więckowski et al 1999;
164 Darve and Laouafa, 2000; Bardenhagen & Kober 2004; Conte et al 2010; Andersen & Andersen,
165 2010; Pinyol et al 2011; Zabala and Alonso 2011; Yerro et al 2014; Alonso et al 2014) may
166 describe the deforming mass by elastoplastic constitutive equations familiar in Soil Mechanics.
167 DEM and related procedures describe the moving mass by laws of interaction between
168 particles or blocks (Cleary and Campbell 1993; Campbell et al 1995).

169 If the main deformation mechanism considered is one of sliding along localized and thin
170 shearing surfaces, the underlying assumption is that these surfaces are already fully
171 developed. Of the four different types of slope movements described by Leroueil (2001) we
172 are thus concerned with the post-failure stage following first-time failures, which includes the
173 movement of the sliding mass from immediately after the full development of the shearing

surface till it comes to rest, and with reactivated slides, where movement restarts along a pre-existing failure surface developed during a past event. It is physical and physicochemical processes occurring at these shearing surfaces that determine the slide's motion and its evolution in time. However, the enormous difference of scale between the thickness of the shearing band and that of the slide raises difficulties. Integration of both scales in a common calculation procedure requires a trade-off, as methods providing a reasonable description of the entire moving mass are ill-conditioned to describe complex physical mechanisms at the scale of a shearing band. However, a combination of simple dynamic equilibrium models for the entire slide and closer attention to the deforming shearing bands proves useful. This is the approach followed here, in line with Voight and Faust (1982), Hendron and Patton (1985), Vardoulakis (2002), Veveakis et al (2007), Pinyol and Alonso (2010a, 2010b), Goren and Aharonov (2009), Cecinato et al (2011), Cecinato and Zervos (2012). In all these cases the heat generated by friction and the resulting pressurization of interstitial water were fundamental parts of the analysis; their relevance in explaining high landslide velocities was first highlighted in the pioneering contributions of Habib (1975); Uriel and Molina (1977) and Voigt and Faust, (1982). Table 1 summarizes the main aspects of published contributions on thermal effects and rapid landslide triggering.

The scope of the paper is limited to landslides whose evolving geometry is characterized by soil or rock masses that essentially maintain their original bulk stiffness and strength. The motion is explained by localized shearing surfaces such as those often located in clayey strata described as indurated claystones or overconsolidated clays. Interestingly, Tang et al (2009) observe that, despite the heavy internal fracturing observed in many large landslides, they show a "remarkable tendency to remain in a more or less unchanged sequential order"; this helps extend the analysis described here to a larger class of landslides.

From a geotechnical perspective, it is important to distinguish between first-time failures and reactivation of ancient landslides. The first type develops in "intact" sites. They are difficult to analyze, especially when brittle materials are involved in the vicinity of the potential failure surface, as is the case of hard soils or soft argillaceous rocks, in particular those of high plasticity. The strength operating in practice and the geometry of the failure surface are difficult to predict because the failure mechanism develops progressively. Early classic studies on this topic were published by Skempton et al. (1967), Bjerrum (1967) and Bishop (1967, 1971). More recent contributions include those by Cooper (1998), Potts *et al.* (1990), Dounias *et al.* (1990), Mesri and Shahien (2003), Gens and Alonso (2006) and Zabala and Alonso (2010).

In contrast, re-activated ancient landslides occur on a pre-existing sliding surface that has been subjected to an increasing history of accumulated relative displacements. Hence, it is expected that cohesion will be insignificant on the sliding surface and the friction angle will be close or equal to residual values. It is widely accepted that ancient landslides exhibit a low safety factor close to conditions of strict equilibrium (SF=1). ICOLD (2002) reports that in at least 75% of cases where old landslides (active or inactive) are disturbed, e.g. by an excavation or by submerging the toe, slide reactivation or an increase in velocity is observed. It is also frequently observed, especially in consolidated clayey strata, that a very low value of friction angle, even lower than the residual friction determined in ring shearing tests, operates in joints and shearing zones of ancient landslides. The evolution of residual strength during resting times is a controversial subject which has been discussed in Alonso and Pinyol (2014).

Consider, as an introduction to the remainder of the paper, the motion of a block sliding on a friction-resistant surface inclined at angle β. Velocity increases linearly with time, *t*, following the equation:

$$v = g \sin\beta \left(1 - SF\right) t \qquad (1)$$

where *g* is the gravity acceleration and *SF* the initial safety factor, defined as the ratio between resisting (shear strength) and disturbing shear stress. If SF=1.0 the block remains still. To initiate motion it is necessary to introduce some imbalance between resisting and disturbing stress. In real situations involving re-activated slides the imbalance may have different origins but it is typically small; e.g. raising the water level in a reservoir slowly affects pore pressures in the valley upstream.

For SF=0.99 and β=10º, equation (1) predicts that a catastrophic sliding velocity of 1m/s will be reached in 58s. However field evidence does not support this result. A reasonable explanation is that the friction angle increases slightly as slide motion causes the rate of shearing on the failure plane to increase. Then *SF* increases to *SF*=1 and the slide reaches dynamic equilibrium and exhibits creeping motion, i.e. it moves with constant or near-constant velocity that is also relatively low.

Experience also indicates (this is the case of Vaiont) that a relatively slow creep motion of a few mm/day may evolve to 30m/s in 15s. However equation (1) predicts, for the same slope angle, that for a small reduction of *SF* by 1% it takes 30 minutes to reach 30m/s. Therefore equation (1) is unable to explain observations at the two scales of the motion of interest in practice: the creeping states and the eventual catastrophic outcome.

Material brittleness may explain a significant reduction of shear strength at the start of the motion. It may be invoked in cases of first time failures but it cannot be easily justified in re-activated slides or in creeping motions that may evolve into a rapid slide. It may be also present in compound sliding motions which require shearing across “intact” rock and not only on the basal sliding surface. This is certainly an acceptable scenario in some cases but it cannot explain the rapid motion of planar slides, which is a common case.

245 This paper is organized as follows: The question of the strain rate dependence of friction is
246 discussed in Section 2. In Section 3 a thermo-poro-mechanical model for an infinite planar slide
247 is presented, using appropriate dimensionless variables. Section 4 discusses the numerical
248 methods developed to solve the corresponding initial/boundary value problem, and Section 5
249 contains a range of numerical results that provide insights into the underlying phenomena.
250 Some conclusions are presented in Section 6.

251

252 ## 2. STRAIN RATE DEPENDENT FRICTION AND PRECURSORY SLIDING MOTIONS

253 Before discussing some results of shearing experiments it is convenient to briefly examine
254 some basic concepts of the theoretical understanding of friction. The initial contributions are
255 presented in Bowden & Tabor (1964). Mitchell (1976) and Rice (2001) describe how employing
256 the theory of "activation energy" at the level of microscopic contacts leads to the common law
257 of friction. A frictional contact is idealised as a number of isolated contact points (Fig. 1) where
258 adhesion (τ_c) and normal stresses (σ_c) are understood to act at the scale of molecular
259 interactions between the minerals in contact. Normal and shear stresses are expected to reach
260 high local values and are controlled by chemical reactions. Using equilibrium, the macroscopic
261 shear and normal stresses (τ and σ) are related to their microscopic counterparts as:

262 $$\tau = \sigma \frac{\tau_c}{\sigma_c} \qquad (2)$$
263

which justifies why shear stress is linearly related to normal stress.

264 However, under transient shearing, chemical reactions at the molecular scale of the isolated
265 process zones of the local contacts are expected to change the value of the adhesion stresses
266 (τ_c). If local chemical reactions follow a rate process, their velocity of reaction can be written:

267 $$v = v_1 \exp\left(-\frac{E}{RT}\right) \qquad (3)$$

where E is the activation energy, T is absolute temperature, R is the gas constant and v_1 is a reference shearing rate. The interpretation of this equation is that the energy E in equation (3) allows a shearing rate velocity v. E has the meaning of a threshold energy barrier: if it decreases, velocity increases. Applied stresses decrease the energy barrier and increase the velocity of the processes taking place at the point contacts and, therefore, the velocity of deformation. Stress is understood as energy per unit volume, so the effect of stress on the energy barrier E can be expressed as:

$$E = E_1 - \tau_c \Omega \qquad (4)$$

where Ω is an active volume of contact bonds and E_1 is a reference energy barrier. Equations (3) and (4) lead to

$$\tau = \sigma \left[\frac{E_1}{\Omega \sigma_c} + \frac{RT}{\Omega \sigma_c} \ln \frac{v}{v_1} \right] \qquad (5)$$

which predicts a linear increase of friction with the logarithm of shearing velocity. The reference term $E_1/(\Omega\sigma_c)$ is interpreted as a basic friction which may depend on the state of the frictional surface; "state" may include shearing relative displacement, applied stress and time (Rice et al, 2001). The friction law may then be written,

$$\frac{\tau}{\sigma} = f = f^* + \bar{\psi} + A \ln \frac{v}{v^*} \qquad (6)$$

where f^* is a basic friction and $\bar{\psi}$ includes effects other than those associated with shearing velocity.

Experimental results at low shearing rates tend to support equation (6). For instance, based on direct and ring shear tests of highly plastic clay layers of the Clearwater formation in Alberta, Canada, Wedage et al. (1998) proposes the following empirical relationship between residual friction and shearing rate:

291 $$\tan\phi = \tan\phi_0 \left(1 + a \ln \frac{\dot{\varepsilon}}{\dot{\varepsilon}_0} \right) \quad (7)$$

292 Cooper et al (1999) investigated the effect of rate of shear on ring shear tests performed on
293 high plasticity Gault clay. Shearing rates varied almost four orders of magnitude, from 0.5
294 mm/min to 0.0001 mm/min, but still within the range expected in creeping slide motions. Tika
295 et al (1996) extended the rate of shearing to the range 10^{-5} to 10^{4} mm/min and concluded that
296 the evolution of residual strength depends on the type of soil. They found that some soils
297 exhibit a "negative" rate effect of the residual strength, which was explained as result of an
298 increase in water content in the shear zone, because of the dilatant effect of "turbulent"
299 shearing (which requires some granular content). Skempton (1985) presented results of ring
300 shear test on clays conducted at rates from 100 times faster to 100 times slower than the
301 commonly used 0.01mm/min; they show that the residual strength increased by about 2.5%
302 per log cycle increase in strain rate, an increase that Skempton (1985) acknowledges can cause
303 large changes in the rate of movement.

304 Direct shear tests on polished surfaces of rock (Dieterich, 1979, Ruina, 1983) support a linear
305 increase of the friction coefficient with the logarithm of the shearing rate. Alternative
306 proposals have also been presented, e.g. Davis *et al*. (1993) propose:

307 $$\frac{\tau}{\sigma} = f = f^* + b \frac{v}{v_r} \exp\left(\frac{-v}{v_r} \right) \quad (8)$$

308 The velocity term in Equation (8) provides an initial increase in friction with velocity followed
309 by a decrease for $v > v_r$.

310 Testing devices capable of shearing soil samples to velocities in excess of 0.1 m/s have been
311 developed in the past decade. Temperature in these tests rises to values that can cause
312 transformation of minerals. As a rough guide, montmorillonite loses water molecules from
313 interlayers at temperatures <200 ºC; kaolinite loses water and transforms into a complex

amorphous structure of aluminum and silica compounds at about 550ºC and calcite transforms into CaO and releases CO_2 gas at temperatures of 600ºC - 850ºC.

Ujiie and Tsutsumi (2010) report the results of tests performed on clayey gouges in a rotary shear apparatus capable of measuring the shearband temperature. In saturated samples, temperature increase and reduction of apparent friction under high shearing velocity (in excess of 0.1mm/s) develop in tandem. The authors attributed the loss of friction to the thermally induced dilation of water and concluded that mineral de-hydration and water vaporization were not responsible for the rapid "slip weakening" observed. For shearing rates below 0.1 mm/s it was found that the clay gouge exhibited friction strengthening; this is consistent with data reported by Tika et al (1996).

Many authors have reported in recent years the results of high velocity shearing (limited to around 1.3m/s in most cases) in a variety of soil types (Di Toro et al, 2006; Mizoguchi et al, 2007; Ferri et al, 2010; Liao et al 2011; Han and Hirose, 2012; Yang et al, 2014) tested both saturated and unsaturated. The soils tested are typically a mixture of quartz, carbonate minerals and clay minerals. Pore pressures and temperatures were, apparently, never measured. These tests as well as field observations (e.g. the presence of sheared mud in joints adjacent to the main shearing surface; the observation of molten rock injected from the sliding surface into the fault after earthquakes) indicate that the shearing strength reduction may have the following origins: grinding of minerals into nanoparticles of low friction; de-hydration of minerals and the associated increase in pore pressure; de-carbonation of calcite and the release of pressurized gas; melting of minerals, resulting in a viscous material and thermal pressurization because of the different dilation coefficients of water and minerals, in the case of saturated soils. Lack of saturation enhances the transformation of clay minerals and the release of CO_2, which is an indication of unsaturated samples attaining higher temperatures compared with saturated ones. The results can be explained by considering that saturation

allows the reduction of normal effective stress to very small values, in turn reducing heat production despite the high shearing rate. This is consistent with the results of Ujiie and Tsutsumi (2010) mentioned above.

Shearing rates in creeping slides are not expected to exceed 0.1-1 mm/s in practice. Therefore the notion of creeping can be explained by friction strengthening with increasing shearing rate, without the need to invoke the concept of viscosity. On the other hand, the extension of friction-rate relationships such as equations (6), (7) or (8) to high shearing rates is more uncertain.

The question of the transformation of a creep motion into an accelerated motion eventually leading to failure has also been approached from a different perspective. Monitoring of slope deformations suggests that the time to failure may be predicted by relating linearly the inverse of velocity with time (Saito, 1965, 1969; Voight, 1978). Helmstetter et al (2003) discuss the rationale behind these procedures. They further examine the effect of friction strain rate and state dependence by considering the dynamics of a simple sliding block in conjunction with the friction law given by equation (6), elaborated as:

$$\mu = \mu_0 + A\ln\frac{\dot{\delta}}{\dot{\delta}_0} + B\ln\frac{\xi}{\xi_0} \qquad (9)$$

where μ is the friction coefficient, $\dot{\delta}$ is the sliding velocity, ξ a state variable, subscript 0 refers to reference values and *A* and *B* are model parameters. The evolution of the state variable is given by:

$$\frac{d\xi}{dt} = 1 - \frac{\xi\dot{\delta}}{D_c} \qquad (10)$$

where D_c is interpreted as a critical size of asperities of the shearing surface. Variable ξ may model strengthening actions (aging, for instance) or weakening effects for accumulated shear displacements. The authors concluded that the stability of the motion is controlled by the ratio *B/A*: *B/A* > 1 leads to instability, where the slope velocity increases continuously. They suggest

363 that this was the case of Vaiont. If 0 < *B/A* < 1 the motion remains stable and the velocity may
364 increase or decrease towards a constant value. They suggest that this is the case of La Clapière
365 (Follacci et al, 1993). The result is very attractive because it seems to provide a simple and
366 elegant solution to a complex problem. However, this model is unable to explain the fast
367 acceleration of the landslide once it has initiated, i.e. the transition from pre-failure velocities
368 of the order of 4cm/day to a final velocity of 30m/sec in an estimated time of 15s. It is
369 concluded that a different physical phenomenon should be explored if such acceleration is to
370 be captured. The situation is sketched in Figure 2. The rate and state dependent laws of
371 friction seem to be capable of predicting creeping behaviour and even a (slow) transition
372 towards failure (a phenomenon also known as tertiary creep). But they are not capable of
373 explaining very fast slide accelerations starting at a state of creeping velocities. Modelling this
374 transition is the subject of the next section.

375 In the remaining of this paper the following rate dependent friction angle will be used:

376 $$\tan\phi = \tan\phi_0 \left(1 + A \ln \frac{v}{v_0}\right) \qquad (10)$$

377 where v is the sliding velocity across the shear band and v_0 is a reference velocity.
378 Interpretation of the reported results on residual friction of clayey soils indicates that the rate
379 parameter A can be taken to vary between extremes of 10^{-5} and 10^{-2}. For a baseline friction
380 of $12°$ and a reference velocity $v_0 = 0.01mm/min$, this range implies that a four-orders-of-
381 magnitude increase of velocity will lead to an increase in the residual friction angle between
382 $0.01°$ for $A = 10^{-5}$, which is negligible, and $5.7°$ for $A = 10^{-2}$, which represents an extreme,
383 near-50% increase over the baseline value.

3. A THM STRAIN RATE DEPENDENT SLIDING BLOCK MODEL. PROBLEM FORMULATION

Problem Description

Consider a slope inclined an angle β and a planar landslide with constant thickness D (Fig. 3). The sliding mass moves as a rigid body and deformations concentrate in a shear band of thickness 2*e* parallel to the slope surface (Fig.3). The shearing zone is a large planar surface compared with the band thickness, undergoing uniform deformation. A linear profile of shearing velocity inside the band is assumed. Temperature and pore pressure build-up will be concentrated into the shear band and its vicinity. Therefore the analysis may be formulated as one-dimensional in the direction normal to the band. Water and energy transfer become one-dimensional processes along the spatial coordinate *z* (Fig.3). The band thickness is typically small, in the range of a few mm or cm. Shear bands in real cases are often embedded in thicker layers of claystone or clay bearing rocks, whose properties the band material may be assumed to share.

Water flow parallel to the slope, over height h_w above the sliding plane, is assumed (Fig. 3).

Dimensionless Governing Equations

The landslide motion is described using the dynamics equation. Acceleration results from the difference between gravitational driving forces and frictional resistance forces along the shear band. Frictional forces are controlled by the pore water pressure which is equal to the sum of the initial pore water pressure, present before movement initiates, and any excess pore water pressure generated during sliding due to shearing induced heating. Pore pressure and heat dissipation occur simultaneously and are governed by the corresponding mass and energy balance equations inside and outside the shear band.

The following dimensionless variables have been selected to write the governing equations:

408 $$\hat{z}=\frac{z}{D},\ \hat{t}=\frac{t\sqrt{gD}}{D},\ \hat{\theta}\left(\hat{z},\hat{t}\right)=\frac{\theta\left(z,t\right)}{\theta_0},\ \hat{u}_w\left(\hat{z},\hat{t}\right)=\frac{u_w\left(z,t\right)}{\rho gD},\ \hat{p}_w=\frac{p_w}{\rho gD},\ \hat{v}\left(\hat{t}\right)=\frac{v\left(t\right)}{\sqrt{gD}} \quad (11)$$

409 where t is the time, θ the temperature, u_w the excess pore water pressure, p_w the initial pore
410 water pressure and v the landslide velocity. $\rho = n\rho_w + (1-n)\rho_s$ is the density of the
411 saturated soil, expressed in terms of porosity, n, and the densities of water ρ_w and solid
412 particles ρ_s. g is the gravitational acceleration and θ_0 is a reference initial temperature,
413 assumed equal to 10ºC in the calculations reported below. The governing equations and initial
414 and boundary conditions of the problem are expressed as follows:

415 *Dynamic equilibrium*:

416 $$\frac{d\hat{v}\left(\hat{t}\right)}{d\hat{t}}=\sin\left(\beta\right)-\left(\cos\left(\beta\right)-\frac{\hat{p}_{wh}}{\cos\left(\beta\right)}-\frac{\hat{u}_w^{\max}\left(\hat{t}\right)}{\cos\left(\beta\right)}\right)\tan\varphi' \quad (12)$$

417 Initial condition: $\hat{v}\left(\hat{t}=0\right)=0$

418 *Energy balance equation:*

419 $$\frac{\partial\hat{\theta}\left(\hat{z},\hat{t}\right)}{\partial\hat{t}}-\frac{\Gamma}{\left(\rho c\right)_m D\sqrt{gD}}\frac{\partial^2\hat{\theta}\left(\hat{z},\hat{t}\right)}{\partial\hat{z}^2}=\hat{H}\left(\hat{z},\hat{t}\right) \quad (13)$$

420 where

421 $$\hat{H}\left(\hat{z},\hat{t}\right)=\frac{\rho gD^2}{\left(\rho c\right)_m\theta_0 2e}\left(\cos^2\left(\beta\right)-\hat{p}_{wh}-\hat{u}_w^{\max}\left(\hat{t}\right)\right)\tan\varphi'\hat{v}\left(\hat{t}\right)\ \text{for}\ \hat{z}\in\left[0,e/D\right] \quad (14a)$$

422 $$\hat{H}\left(\hat{z},\hat{t}\right)=0\ \text{for}\ \hat{z}\in\left(e/D,L_\theta\right] \quad (14b)$$

423

424

425

426

427 Initial and boundary conditions are given by:

$$\begin{cases} \hat{\theta}\left(\hat{z},\hat{t}=0\right)=1 & (15a) \\ \left.\dfrac{\partial\hat{\theta}}{\partial\hat{z}}\right|_{\left(\hat{z}=0,\hat{t}\right)}=0 & (15b) \\ \hat{\theta}\left(\hat{z}=e^{-}/D,\hat{t}\right)=\hat{\theta}\left(\hat{z}=e^{+}/D,\hat{t}\right) & (15c) \\ \left.\dfrac{\partial\hat{\theta}}{\partial\hat{z}}\right|_{\left(\hat{z}=e^{-}/D,\hat{t}\right)}=\left.\dfrac{\partial\hat{\theta}}{\partial\hat{z}}\right|_{\left(\hat{z}=e^{+}/D,\hat{t}\right)} & (15d) \\ \hat{\theta}\left(\hat{z}=L_{\theta}/D,\hat{t}\right)=1 & (15e) \end{cases}$$

428 The specific heat of the saturated porous medium is calculated using a weighted average:
429 $\left(\rho c\right)_m=n\rho_w c_w+\left(1-n\right)\rho_s c_s$ where c_w and c_s is the specific heat of water and solid particles
430 respectively. Fourier's thermal conductivity is also calculated as a weighted average
431 $\Gamma=n\Gamma_w+\left(1-n\right)\Gamma_s$, where Γ_w and Γ_s the conductivity of water and solid respectively. In line
432 with (Alonso and Pinyol, 2010b), advective heat transfer is neglected.

433 The dimensionless source term $\hat{H}\left(\hat{t}\right)$ in equation 14a quantifies the heat input into the shear
434 band in terms of the work consumed per unit volume of the material by its shear strength.
435 Outside the band, where the mass moves as a rigid body, no heat is generated (eq. 14b).

436 Regarding initial and boundary conditions, the first condition (eq. 15a) imposes that initially
437 the shear band and surrounding zone are at the reference temperature. No heat is transferred
438 across the center of the shear band and therefore no heat flow is imposed at $\hat{z}$ =0 (eq. 15b).
439 Continuity of temperature and temperature flow should be satisfied on both sides of the shear
440 band (eq. 15c and 15d). The temperature boundary condition at $\hat{z}=L_{\theta}/D$ (eq. 15e) stipulates
441 that temperature remains unaffected beyond a pre-determined distance L_{θ} from the axis of
442 the shear band. If taken further away from the shear band than heat flow will reach during the
443 time frame modelled, L_{θ} does not affect the results.

444 *Mass balance equation:*

445 $$-\frac{\beta_{soil}\theta_0}{m_{soil}\rho g D}\frac{d\hat{\theta}\left(\hat{z},\hat{t}\right)}{d\hat{t}}+\frac{d\hat{u}_w\left(\hat{z},\hat{t}\right)}{d\hat{t}}-\frac{k}{\gamma_w m_{soil} D\sqrt{gD}}\frac{d^2\hat{u}_w\left(\hat{z},\hat{t}\right)}{d\hat{z}^2}=0 \quad (16)$$

446 Initial and boundary conditions are given by:

$$\begin{cases} \hat{u}_w\left(\hat{z},\hat{t}=0\right)=0 & (17a)\\ \left.\dfrac{\partial\hat{u}_w}{\partial z}\right|_{\left(\hat{z}=0,\hat{t}\right)}=0 & (17b)\\ \hat{u}_w\left(\hat{z}=e^-/D,\hat{t}\right)=\hat{u}_w\left(\hat{z}=e^+/D,\hat{t}\right) & (17c)\\ \left.\dfrac{\partial\hat{u}_w}{\partial z}\right|_{\left(\hat{z}=e^-/D,\hat{t}\right)}=\left.\dfrac{\partial\hat{u}_w}{\partial z}\right|_{\left(\hat{z}=e^-/D,\hat{t}\right)} & (17d)\\ \hat{u}_w\left(\hat{z}=L_{u_w}/D,\hat{t}\right)=0 & (17e) \end{cases}$$

448 In the mass balance equation (16), β_{soil} is a weighted average thermal expansion coefficient for
449 saturated soils calculated as: $\beta_{soil}=n\beta_w+(1-n)\beta_s$, where β_w and β_s are the thermal expansion
450 coefficients of water and solid particles respectively. These depend on temperature, e.g.
451 Wagner and Kruse (1998); however as a first approximation they are assumed here to be
452 constant. m_{soil} is the compressibility of saturated soil, calculated as $m_{soil}=m_v+n\alpha_w$ where m_v
453 and α_w are the coefficients of compressibility of the soil skeleton and the water respectively.
454 k is the saturated permeability of the soil.

455 Initial and boundary conditions are similar to those imposed for heat transfer. The initial value
456 of excess pore pressure is zero (eq. 17a). No water flow crosses the center of the shear band
457 (eq. 17b). Equations 17c and 17d ensure continuity of excess pore pressure and flow rate on
458 both sides of the band. The excess pore pressure is assumed zero beyond a pre-determined
459 distance L_{u_w}. If this distance is far enough for excess pore pressure to not develop there, it
460 does not affect the results; otherwise it stipulates the existence of a drainage boundary.

L_θ and/or L_{u_w} may be interpreted as the thickness of the claystone layer containing the shear band: pore pressure and temperature should be maintained constant at its outer boundary. Alternatively, if the layer is in contact with a pervious rock mass, it is reasonable for these conditions to apply at the interface.

Four dimensionless coefficients are naturally defined in the balance and equilibrium equations. They are associated with the physical phenomena describing the problem:

$\Theta = \frac{\Gamma}{(\rho c)_m D\sqrt{gD}}$, coefficient associated with heat flow in the heat balance equation;

$\Psi = \frac{\rho g D^2}{(\rho c)_m \theta_0 2e} = \frac{\rho D(\sqrt{gD})^2}{(\rho c)_m \theta_0 2e}$, coefficient of the source term in the heat balance equation;

$\Pi = \frac{\beta_{soil}}{m_{soil}} \frac{\theta_0}{\rho g D}$, coefficient associated with thermal expansion of porous rock in the mass balance equation of water;

$\Sigma = \frac{k}{\gamma_w m_{soil} D\sqrt{gD}}$, coefficient associated with stress induced volumetric deformation in the mass balance equation of water;

Θ is a measure of the thermal dissipation and combines thermal conduction, heat storage, a reference dimension and a reference velocity; Ψ can be interpreted as the ratio between the kinetic energy of the moving mass and the initial heat stored in the shear band, Π is a ratio of the thermal expansion of the saturated porous medium with respect to its mechanical compressibility and Σ is a dimensionless consolidation coefficient that combines permeability, confined compressibility and the sliding depth.

For a given planar landslide of thickness *D*, the range of variation of the non-dimensional parameters is limited. Properties such as density, Fourier's coefficient, thermal expansion

coefficient and the specific heat for common soils and rocks exhibit small variation especially if compared with other parameters such as permeability. Typical values for these material properties are indicated in **Error! No s'ha trobat l'origen de la referència.**. On the contrary, permeability, k, soil compressibility, m_v, and thickness of the shear band, e, may change more significantly. Typical ranges of values of these variables are collected in **Error! No s'ha trobat l'origen de la referència.**. As a consequence, the dimensionless parameters that may vary significantly depending on the particular case analyzed are: Ψ which is inversely proportional to the band thickness; Π which is inversely proportional to the band compressibility coefficient; and Σ which depends on the ratio of permeability and soil compressibility.

Using **Error! No s'ha trobat l'origen de la referència.** and **Error! No s'ha trobat l'origen de la referència.**, ranges for the values of the non-dimensional parameters can be established. Θ is essentially constant and equal to $1.27 \cdot 10^{-9}$. Ψ depends on the shear band thickness and may vary between 30 and 1800. Π may vary by two orders of magnitude, roughly between 0.1 and 10, due to the variability of the shear band compressibility coefficient. Finally, Σ depends on the ratio between permeability and compressibility so its range of variation is much wider, between 10^{-3} and 10^{7}. Shear bands are often located in highly overconsolidated layers having a wide range of clay mineral content. Their compressibility will be closer to the medium and low values within the range indicated in Table 2, reducing the variability mainly of Π but also of Σ in practice. Permeability remains as the main source of variability.

Zero thickness shear band

Idealizing the sliding surface as a zero thickness shearing band may be sufficiently close to actual conditions, especially in highly plastic materials where sliding surfaces are often described as smooth and polished planes. In terms of problem formulation and its numerical solution, the hypothesis of zero band thickness presents some advantages: a) the geometry is simplified and one of the parameters entering the dimensionless formulation, the band

thickness, 2*e*, disappears and b) the discretization of the domain is simplified because there is no need to discretize the very thin band.

The rate of frictional work expended along the contact plane, per unit of surface, is now calculated as the product between shear strength and velocity. This mechanical work dissipates into heat that enters the rock mass. With reference to Figure 1, when 2*e*=0, the coordinate *z*=0 indicates the position of the contact plane.

The system of equations governing the problem is similar to the system for finite band thickness. The difference lies in the heat balance equation, which becomes:

$$\frac{\partial\hat{\theta}\left(\hat{z},\hat{t}\right)}{\partial\hat{t}}-\frac{\Gamma}{\left(\rho c\right)_m D\sqrt{gD}}\frac{\partial^2\hat{\theta}\left(\hat{z},\hat{t}\right)}{\partial\hat{z}^2}=0$$

with the following initial and boundary conditions:

$$\begin{cases}\hat{\theta}\left(\hat{z},\hat{t}=0\right)=1\\ \left.\dfrac{\partial\hat{\theta}}{\partial\hat{z}}\right|_{\left(\hat{z},\hat{t}=0\right)}=0\\ \dfrac{1}{2}H\left(\hat{t}\right)=-\dfrac{\Gamma\theta_0}{D}\left.\dfrac{\partial\hat{\theta}}{\partial\hat{z}}\right|_{\left(\hat{z}=0,\hat{t}\right)}\Rightarrow\dfrac{\partial\hat{\theta}}{\partial\hat{z}}_{\left(\hat{z}=0,\hat{t}\right)}=-\dfrac{\rho gD^2\sqrt{gD}}{2\Gamma\theta_0}\left(\cos^2\left(\beta\right)-\hat{p}_{wh}-\hat{u}_w^{\max}\left(\hat{t}\right)\right)\tan\varphi'\hat{v}\left(\hat{t}\right)\\ \hat{\theta}\left(\hat{z}=L_0/D,\hat{t}\right)=1\end{cases}$$

Note that no heat is generated in the sliding mass, but heat flow is imposed through a boundary flux at $z=0$. Because of symmetry only half of the heat generated is considered. The dimensionless parameters describing this problem remain identical to the case of finite band thickness except for the coefficient associated with the source term in the heat balance equation, which becomes $\Psi=\dfrac{\rho gD^2\sqrt{gD}}{2\Gamma\theta_0}$. The heat generated at the boundary is now calculated as:

$$H\left(\hat{t}\right)=\rho gD\sqrt{gD}\left(\cos^2\left(\beta\right)-\hat{p}_{wh}-\hat{u}_w^{\max}\left(\hat{t}\right)\right)\tan\varphi'\hat{v}\left(\hat{t}\right)$$

Rate effects

Slow maintained slide displacement rates (creeping) will be explained by considering strain rate effects on strength, following the discussion in Section 2. The analysis concentrates on active slides irrespective of their initial creeping rate; therefore frictional strength is characterized by a residual friction angle. The effective residual friction strength is defined as the sum of the strength available at velocities lower than a given value of reference (v_{ref}) and an additional term that depends on sliding velocity:

$$\tan\phi = \tan\phi_0 + f_v \tag{18}$$

Recalling the logarithmic law of Equation (10):

$$f_v = A\ln\left(\frac{v}{v_{ref}}\right) = A\ln\left(\hat{v}\frac{\sqrt{gD}}{v_{ref}}\right) \text{ for } v > v_{ref}\,;\hat{v} > \hat{v}_{ref} = v_{ref}/\sqrt{gD} \tag{19a}$$

$$f_v = 0 \text{ for } v \le v_{ref}\,;\hat{v} \le \hat{v}_{ref} = v_{ref}/\sqrt{gD} \tag{19b}$$

The slope angle β and the parameters defining the friction law (φ_0', A, $v_{ref}/\sqrt{gD}$) complete the set of dimensionless parameters governing the problem.

4. NUMERICAL INTEGRATION

Equations (12), (13) and (16) form a system of coupled, non-linear partial differential equations that needs to be solved. The use of centred-space forward-time (explicit) finite differences has been the norm in past work (e.g. Vardoulakis, 2002, Alonso et al, 2010, Cecinato et. al. 2011, 2012). However explicit integration requires very small timesteps, typically of the order of 10^{-5}sec, for numerical stability. Although acceptable when modelling the catastrophic phase of a slide over its final few tens of seconds, this onerous condition makes modelling of the long-term creep behaviour that may precede failure impractical. The alternative we explore here is

544 the use of an unconditionally stable implicit scheme that will allow much larger timesteps. The
545 ability to adapt the timestep during the calculation is also essential, so that long periods of
546 creep where the solution changes by very little can be modelled efficiently. We use here the
547 trapezoidal rule, which is of order $O(\Delta t^2)$. In principle it is also possible to use a higher order,
548 more accurate multistep method; however adaptive time stepping will only be possible at the
549 cost of significantly increased complexity, e.g. Skeel (1986).

550 The resulting system of equations must be solved iteratively to calculate at the end of each
551 timestep the slide velocity as well as the temperature and excess pore pressure everywhere in
552 the domain. Solution using a full Newton-Raphson method is however problematic, as the
553 logarithmic friction law renders the dynamics equation highly nonlinear. Convergence requires
554 timesteps typically smaller than 10^{-3}sec, defeating the purpose of the implicit scheme.

555 The strategy adopted was to use a staggered solution scheme: the diffusion equations were
556 solved by Newton-Raphson using the current approximation of the velocity; the dynamics
557 equation was subsequently solved by Pegasus (Dowell and Jarratt, 1972), a method of the
558 *regula falsi* family that is known to be fast and efficient in finding roots of nonlinear equations.
559 Iterations continued till the residuals of all equations were below tolerance. The timestep was
560 increased or decreased based on the rate, or lack of, convergence. The maximum timestep
561 used was 24h. This approach allowed timesteps of the order of 10^5sec for the most part of an
562 analysis, making the efficient modelling of years of creeping motion possible.

563 An additional challenge was the location of the far boundary L_θ and L_{u_w}. Previous work
564 considered that ambient values of temperature and excess pore pressure are applicable at a
565 distance equal to a small multiple of the shearband thickness. Although this is valid for rapid
566 heat generation during the final collapse, modelling the creep phase should require a larger
567 domain, as heat and pore water will potentially have the time to travel longer distances. In
568 practice, the presence of a geological feature, such as an interface with pervious rock, may

provide a natural boundary within the sliding mass, as discussed previously. For the general case, however, the following numerical approach was adopted: The far boundary was initially considered at a distance 10 times the shearband thickness. If, during the calculation, the value of either the temperature or the excess pore pressure next to the boundary was found to differ by more than 10^{-10} ^{0}C or kPa respectively from the corresponding boundary condition, the domain was expanded by 100 times the shearband thickness before the calculation continued. Therefore the problem progressively became computationally more expensive; typical calculations started with about 300 unknowns but eventually involved in excess of 300,000. Nevertheless, due to the direct, sparse multi-frontal solver (HSL, 2015) used, all models could run on a desktop computer within hours.

5. ANALYSIS

5.1 An illustrative example

The case presented below illustrates the capability of the model to integrate a history of creeping motions and the eventual triggering of a rapid catastrophic motion. Basic parameters are given in Table 1. The sliding mass is defined by D=25m, h_{w0} =11.05m, β=9.8º, ϕ_0=12º, 2e=2.5mm, m_v=1.5.10^{-9}Pa^{-1} and k=10^{-9}m/s . The strain rate effect is characterized by A=0.014 and v_{ref}=10^{-5}m/s. An initial temperature θ_0 =10ºC is assumed. The shear band is centered in a clayey layer 2m thick, bounded by pervious rock that is able to maintain the initial pore pressure and temperature.

The slope is initially in strict equilibrium with zero velocity. It is destabilized by increasing the water level to h_w=12m. The subsequent history of water level changes is given in Figure 4a. There is a transient reduction of h_w from 13m to 12.5m and a final increase to 14m. During this final stage the slide suddenly accelerates. Figure 4 provides the calculated evolution of temperature (Fig 4b,c), excess pore water pressure (Fig 4d), velocity (Fig 4e), displacement (Fig

593 4f) and friction angle (Fig 4g). Temperature and excess pore pressure increase in the shear
594 band as soon as the slide becomes unstable. The sliding velocity slowly increases; however
595 strain rate effects contribute to maintaining dynamic equilibrium. The subsequent reduction of
596 water level reduces the sliding velocity and the shear band excess pore pressure and
597 temperature. Similar changes occur to the friction angle, Fig. 4g, because of strain rate effects.
598 It can be considered that the slope maintains a safety factor SF=1 during the entire creeping
599 period.

600 When a further increase of water level to h_w=14 m is imposed at t=15000s, temperature and
601 pore water pressure increase rapidly and strain rate effects are no longer capable of
602 maintaining a state of slow creeping velocity. The slide accelerates because the pore pressure
603 reaches values close to the normal effective stress on the sliding surface, rapidly reducing the
604 frictional resistance there.

605 Thermal pressurization affects the behaviour of the slide throughout. However there is a
606 qualitative change when friction increase, induced by rate effects, is no longer capable of
607 counteracting the strength reduction caused by pore pressure build-up in the shear band. At
608 that time the creeping stage ends and the slope enters a high acceleration and high velocity
609 stage promoted by a thermally-dominated "feedback loop": temperature increase-pore
610 pressure increase-strength reduction-velocity increase-temperature increase. From that point
611 onwards strain rate effects no longer play a significant role in the evolution of the slide.

612 The remainder of this chapter explores the relationship between these two regimes of slope
613 behaviour. They are intimately linked and particular cases characterized by a sliding geometry
614 and material properties would require a specific analysis. However, the simple planar slide
615 offers insights on the creep-fast sliding coupling. The dimensionless formulation also enhances
616 the generality of the conclusions reached.

617 5.2 Velocity regimes in a planar slide

618 Results will be presented for a fixed displacement equal to twice the height of the sliding mass.
619 This is an arbitrary limit, however analyses of longer runouts are unlikely to be representative
620 due to topographical constraints and/or the resulting fragmentation of the sliding mass.

621 Rate independent friction

622 We consider again the previous example, this time with rate independent frictional strength.
623 No creeping stage is now possible. This case serves as a reference for the rate dependent case.

624 The landslide is destabilized by imposing an increment of the dimensionless pore water
625 pressure ($\hat{p}_{wh}$) equal to 0.0016, equivalent to increase the water level in 10 cm. It involves a
626 reduction of the SF from SF=1 to SF= 0.9978.

627 The effect of the shear band thickness is first examined. This parameter only affects Ψ, the
628 dimensionless coefficient of the source term in the energy balance equation. **Error! No s'ha**
629 **trobat l'origen de la referència.** shows the maximum dimensionless velocity for different
630 values of Ψ and Σ and a constant Π=1 value. Since Π remains constant for all the cases
631 analyzed, variation of Σ implies essentially variation of the permeability. The two plots in
632 Figure 5 present the same information in two different ways. The nearly horizontal lines in
633 Figure 5a indicate that the effect of parameter Ψ on the velocity reached is small. This is also
634 apparent from Figure 5b, where the calculated velocities for different band thicknesses
635 essentially overlap. Parameter Ψ directly affects the heat generated in the shear band. The
636 higher its value, i.e. the smaller the band thickness, the larger the quantity of heat generated.
637 However, smaller band thickness also means easier dissipation of the heat and excess pore
638 pressure generated within the band towards the surrounding rock mass. Conversely, a thicker
639 band will produce less heat and excess pore pressure, which will take longer to dissipate. The
640 maximum velocity reached is similar to the calculated velocity for a case in which no thermal
641 effects are included (also plotted in Figure 5). For values of Σ lower than 10^{-7}, no effect of
642 Ψ and Σ is observed and the maximum velocity is the same in all cases. The case of zero

643 thickness shear band is also included in the plot. No significant differences are observed when
644 compared with finite thickness bands.

645 Parameter Σ, which controls the dissipation of excess pore pressure is key in determining the
646 response of the slide. Values of Σ above 10^{-3} result in almost no heat-induced effect. Thermally
647 induced excess pore pressure can dissipate quickly in these cases and frictional strength
648 remains slightly smaller than the initial value. The ratio between the shear strength remaining
649 after the maximum runout has been reached and the initial shear strength is plotted in Figure
650 6. The shear strength essentially vanishes for values of Σ below 10^{-7}, while for values above
651 10^{-3} it maintains its initial value.

652 It is concluded that the effect of the dimensionless parameter Ψ, which essentially varies with
653 the thickness of the shear band, is quite limited.

654 Parameter Σ combines permeability and band compressibility. However the effect of
655 compressibility cannot be accounted for exclusively by Σ because parameter Π is inversely
656 proportional to compressibility: it controls the development of pore pressures for a given heat
657 input, which is an effect independent from pore pressure dissipation, which is governed by Σ.
658 An additional set of calculations were performed to show the combined effect of permeability
659 and compressibility for constant Ψ=345, which corresponds to a shear band thickness
660 2e=5mm. The selected values for parameter Π imply a wide, about two orders of magnitude,
661 range of variability of the soil compressibility. The values of **Error! No s'ha trobat l'origen de la**
662 **referència.** are used for the remaining parameters. The results are plotted in Figure 7.

663 Figure 7 shows, as well as Figure 5b for Π=1, that there is a range of dimensionless
664 consolidation coefficients Σ that separates a high velocity regime (for low Σ values) from a low
665 velocity-, no-heat effect regime (for high Σ values). The observed trends in the variation of
666 velocity with parameter Σ are similar for all Π values. Reducing Π, i.e. increasing band

667 stiffness, decreases the threshold Σ range separating high and low velocity regimes. In other
668 words, given a value of Σ, lower values of Π, which control the heat induced pore water
669 pressure, result in lower sliding velocity.

670 Rate dependent friction

671 Consider now the effect of rate dependent friction. Material properties given in **Error! No s'ha**
672 **trobat l'origen de la referència.** have also been adopted in the cases presented in this section.
673 A base case for discussion is defined by using the frictional law of equations (18) and (19), for *A*
674 = $4.7 \cdot 10^{-3}$ and a reference velocity $\hat{v}_{ref} = 6.4 \cdot 10^{-7}$. The effect of these parameters on the gain in
675 strength with velocity is plotted in Figure 8. This rate dependent law is within the range of
676 experimental results measured at low to moderate shearing velocities (say, below 0.1m/s).
677 Above this velocity thermal pressurization and other phenomena discussed before contribute
678 to the measured rate dependence. However, the plot is extended to high velocities to show
679 the maximum contribution which may be expected from rate effects at high shearing speeds.
680 The parameters chosen imply an increment of 7%, close to one degree, for high sliding velocity
681 (30 m/s). The rate dependent strength increases quickly at low velocity and then levels off.
682 Results for a different value of parameter *A,* used in the discussion below, are also plotted in
683 Figure 8.

684 The slide is destabilised by imposing a 1m increment of the water level. This reduces the SF
685 from 1 to 0.98. Limit equilibrium for this water level is reached for a friction angle equal to
686 12.32º, 2.7% higher than the static friction angle associated with velocities lower than the
687 reference creeping velocity.

688 The base case was analyzed for different values of the Π and Σ parameters. The band
689 thickness-controlled parameter Ψ is considered constant and equal to 345, as its effect has
690 been shown to be insignificant. The results in terms of maximum dimensionless velocity are
691 plotted in **Error! No s'ha trobat l'origen de la referència.**. The case where thermal effects are

692 ignored is added to the figure; in that case dynamic equilibrium is reached for a dimensionless
693 velocity of $4.6 \cdot 10^{-5}$ equivalent to $7.2 \cdot 10^{-4}$ m/s, a reference velocity that depends only on the
694 safety factor attained immediately after the initial instability (Equation 1).

695 When thermal effects are considered, the response observed is similar for the different values
696 of parameter Π selected. A narrow range of Σ values separates fast and slow sliding regimes. If
697 compared with the no-rate-effect case (Figure 5b) the calculated sliding velocities are now
698 higher. This is a consequence of the stronger initial trigger imposed to initiate the slide run-out
699 (Δh_w is now 1 m against Δh_w=0.1m in the previous case).

700 The effect of parameter Π is similar to the effect observed in cases were rate effects were not
701 included. However, the threshold range of Σ values separating the slow and fast sliding
702 regimes decreases when a rate effect on friction is included. This becomes apparent by
703 comparing Figures 9 and 7. In other words, rate effects extend the range of "safe" cases, i.e. of
704 slopes that will not accelerate due to thermal pressurization effects. It appears also that the
705 threshold Σ range is narrower in Figure 9 (rate effects included), compared with Figure 6 (no
706 rate effects)

707 Figure 10 presents the maximum temperature in the centre of the shear band for the cases
708 plotted in Figure 9. If the landslide reaches a high velocity quickly, as is the case for Σ lower
709 than 10^{-9}, the shearband temperature remains relatively low. The temperature also remains
710 low, almost constant, in those cases where the velocity remains low, in a creeping mode, when
711 Σ is higher than 10^{-5}. Maximum values of temperature are reached in intermediate cases,
712 where the excess pore pressure rises relatively slowly and the velocity, although it may
713 eventually become very high, increases at a slower pace. The acceleration of the slide is in fact
714 a critical factor controlling the development of temperature.

715 Increasing the rate dependent component of friction has been shown to have a significant
716 effect in reducing the threshold permeability (through Σ) that leads to a fast sliding regime.
717 This is further shown in Figure 11 where the maximum velocity is plotted in terms of Σ for
718 three *A* values (see Figure 8 for their effect on friction increase). In all cases Ψ=345 and Π=1.0.
719 As expected, the creep velocity when thermal effects are ignored (or Σ has a high value)
720 decreases for increasing *A*. It is noted that for relatively low values of Σ, when excess pore
721 pressure dissipation is slow, the maximum velocity attained is similar in all cases irrespective of
722 the considered rate dependence of friction. When thermal effects develop they dominate the
723 sliding behaviour. However, the development of heat induced pore pressure build-up depends
724 on the creeping history. This relevant issue is discussed in more detail in the next section.

725 5.3 Evolution of motion. Creep-thermo-mechanical interactions

726 Attention is now focused on the effect of the rate of friction increase on the blow-up time, i.e.
727 the time after initiation at which the slope enters a final catastrophic phase. Calculations are
728 performed for a planar slide with D=240m, base friction angle of 12º and slope angle of 9.8º An
729 unbounded domain is assumed and a maximum runout of 2D=480m is considered.

730 To investigate the effect of the rate parameter *A*, a set of analyses is run where the slide is
731 triggered by a minuscule increase of h_w by 0.025% above the strict equilibrium value, resulting
732 to a change in the safety factor $\delta SF = 6 \cdot 10^{-5}$. In the case of rate-independent friction (i.e.
733 *A*=0) catastrophic failure occurs immediately; the slide is classified as “rapid” (IUGS, 1995) 2sec
734 after initiation and, within a few more seconds, frictional heating leads to high temperature
735 and excess pore pressure almost equal to the overburden stress.

736 The introduction of even a very mild rate effect, e.g. $A=10^{-5}$ corresponding to a negligible
737 increase in friction angle by 0.01^0 for a 10^4-fold increase in velocity, suppresses catastrophic
738 acceleration and leads to creep at constant velocity. The magnitude of the velocity attained is

739 governed by the rate parameter A; for A=10^{-5} it is 22cm/day and drops to 1.5cm/day for
740 A=10^{-3}, classifying both slides as "slow" (IUGS, 1995). The temperature increases by 10^0C or
741 less and the excess pore pressure generated is negligible.

742 To further explore the effect of the rate parameter a second set of analyses is run, where the
743 slide is triggered by a more substantial increase of the groundwater level, resulting to
744 $SF = 0.99$. Figure 12 summarises the results.

745 In the case of rate-independent friction A=0 but also for any $A \leq 10^{-4}$, high temperature and
746 excess pore pressure occur almost immediately and lead to catastrophic failure. For
747 $A = 5 \cdot 10^{-4}$ a transitional behaviour is observed, where the slide first creeps with near-
748 constant velocity for the first 15sec before accelerating to catastrophic failure, while for
749 $A > 5 \cdot 10^{-4}$ the slide creeps with "moderate" (IUGS, 1995) constant velocity. Therefore a
750 threshold value A_{crit} of the rate parameter must exist, that determines whether catastrophic
751 acceleration will occur; in this case $6 \cdot 10^{-4} > A_{crit} > 5 \cdot 10^{-4}$. This is further explored using
752 models for a range of values in this interval. Figure 12 shows that even small changes, of the
753 order of 2%, of the rate parameter can have order-of magnitude impact on the duration of the
754 creep phase, although the predicted creep velocity is less sensitive. For comparison, Figure 12
755 also presents the baseline velocity, i.e. the constant creep velocity each slide would attain if
756 thermal effects were ignored: it is evident that, even where thermal effects do not eventually
757 lead to catastrophic collapse, they still increase slide velocity by at least one order of
758 magnitude.

759 It is also interesting to note that it is the *rate* of temperature increase that controls excess pore
760 pressure generation, and thus the associated loss of strength that leads to catastrophic failure.
761 If the time scale of heat generation is large enough the induced excess pore pressures may
762 dissipate before thermal pressurization occurs, irrespectively of how high the temperature
763 attained is. For a given rate of heat production, the rate of excess pore pressure generation

764 will depend on soil permeability. It is thus expected that permeability, therefore the value of
765 parameter Σ, will influence both the creep velocity and the timing of a possible catastrophic
766 failure.

767 To further investigate the impact of parameter Σ, a set of analyses is run with the same trigger,
768 rate parameter $A = 5.75 \cdot 10^{-4}$ and Σ varying between $\Sigma = 6 \cdot 10^{-8}$ and $\Sigma = 6 \cdot 10^{-13}$. The
769 results are summarised in Figure 13.

770 Lower values of Σ lead to faster development of excess pore pressure and earlier onset of a
771 catastrophic phase. As Σ increases so does the duration of the pre-failure creep phase; this
772 relationship is highly nonlinear and, as was the case for the rate parameter, a threshold value
773 Σ_{crit} exists above which a catastrophic phase is never reached. In this case $\Sigma_{crit} \cong 6 \cdot 10^{-11}$;
774 note how, close to that value, increasing the value of Σ by just 2% results to an increase in the
775 duration of the creep phase by a factor of almost three. Figure 13 further shows that, for the
776 parameters used here, the velocity of the slide during the creep phase is essentially unaffected
777 by the permeability; the baseline velocity is again plotted for comparison.

778 Finally, it was found that the maximum temperature that develops in the shearband increases
779 with permeability, regardless of whether a catastrophic phase is eventually reached. This is a
780 direct consequence of the strong influence of permeability on the rate of excess pore pressure
781 generation: the lower the permeability, the faster excess pore pressure rises and effective
782 stress drops, therefore reducing the rate of energy dissipation into heat. Conversely, the
783 higher the permeability the higher the rate of heat production necessary to achieve
784 pressurisation; in fact, models that do not predict a final catastrophic phase consistently attain
785 higher shearband temperature than models that do.

786 5.4. Compound geometry. Creep-thermo-mechanical interactions

Previous sections analyze the landslide evolution including two phenomena that work in opposite directions: the heat-driven acceleration of the landslide and the stabilizing effect of friction rate effects. In a planar geometry the slide remains always in motion. The creeping velocity, away from blowup, depends on the magnitude of the destabilization factors, the intensity of rate effects and additional properties of the shear band, notably its permeability. But other sliding geometries are common. A good example is Vaiont, which may be conceptualized as an evolutionary two-block mechanism (Pinyol and Alonso, 2010b). The sliding motion results in a reduction of the mass of the upper unstable wedge and a parallel increase of the mass of the stabilizing lower wedge. This is a self-stabilizing mechanism unlike the single block case. The effect of this major change in the kinematic description of the landslide is explored here.

Consider the two-block mechanism given in Figure 14. The interaction between the two sliding blocks is given by the axial force on the hinged "rod" connecting the blocks. Changes in water pressure act only on the lower block. In the cases solved both wedges have the same thickness but different initial length. Equations of dynamic equilibrium were written for the two interacting blocks. Balance equations (water flow, energy) were formulated for each of the two blocks, following the previous discussion. A zero-thickness band was adopted in the two blocks. The following example was analyzed: Block thickness, 25 m; the upper and lower blocks have lengths of 60 m and 120 m and slide on a plane inclined 37º and 0º respectively. The remaining physical constants are identical to the planar slides analyzed previously. The stiffness coefficient, m_v=1.5·10^{-9} Pa^{-1}. It leads to the following constant dimensionless parameters for the case analyzed: Θ=1.27·10^{-9}, Ψ=2.72·10^{7} and Π=1. The landslide is destabilised by increasing the water pressure on the sliding surface of the lower block ($\hat{p}_{wh}$ increases by 0.04 which is equivalent to increasing the water level by 1m).

811 The calculated evolution of velocity and run-out if no friction rate effects are considered is
812 given in Figure 15. The effect of Σ , which depends on permeability in the vicinity of the shear
813 band, is highlighted. Low values, below $1.63 \cdot 10^{-7}$ m/s, lead to a slide blowup. This is also the
814 case of a planar slide. However, the main difference of the compound mechanism is that the
815 slide is able to stop, for high band permeability, as a consequence of the weight transfer
816 between upper and lower blocks. Note also that the thermal effect results in some increase of
817 the run-out and velocity if compared with the no thermal pressurization analysis.

818 Friction rate effects, for the same case, are shown in Figure 16 ($A = 4.7 \cdot 10^{-3}$). If conditions lead
819 to thermal blowup, rate effects and slide geometry become largely irrelevant in controlling the
820 sliding velocity and run-out. However, if blowup conditions are not attained, rate effects play a
821 significant role: they reduce the Σ threshold between fast and creeping regimes of the slope
822 and run-out and velocity during the transient motion of the slide after initial instability is
823 significantly reduced. This becomes apparent by comparing Figures 15 and 16.
824

825 6. CONCLUSIONS

826
827 Known cases of rapid landslides can only be explained by negligible shear strength acting on
828 the main failure surface. Among the proposed mechanisms of strength reduction, thermal
829 pressurization of pore water in saturated shear bands may explain a fast accelerated motion as
830 well as a transition from creeping to fast regimes in cases of landslide reactivation. Measured
831 strain rate effects on friction, at low to moderate shearing rates, suggest a linear increase in
832 friction with the logarithm of shearing velocity, a relationship supported by basic friction
833 concepts.

834 A dynamic modelling of landslide motion, which integrates strain rate effects and thermal
835 interactions in a deforming shear band, provides considerable insights into the evolution of the

836 sliding velocity and its eventual blowup, when thermal pressurization dominates the slide
837 motion. A model of this kind, initially developed for planar landslides, has been described by a
838 set of dimensionless balance and equilibrium equations. Four dimensionless constitutive
839 coefficients which control the slide movement were derived. It was found that the shear band
840 permeability and, to a lesser extent, its compressibility, dominate the entire phenomenon.
841 The set of equations require a numerical solution. A novel staggered implicit integration
842 procedure has been proposed. It is capable of handling, within reasonable computational
843 times, a long creeping history and a sudden final blowup.

844 Transition from a slow creeping-like motion to fast acceleration is quite sharp in terms of a
845 dimensionless “consolidation” coefficient which relates band permeability and stiffness as well
846 as the height of the sliding mass. This threshold is significantly affected by friction rate effects
847 in the sense that increasing rate effects reduces the range of shear band properties leading to
848 blowup phenomena. Given a creeping motion of a specific landslide, time to blowup is very
849 sensitive to strain rate effects. Beyond a certain value of the rate parameter, blowup does not
850 seem to be possible within realistic runout distances.

851 The paper also examines the behaviour of compound slide geometries, in particular those
852 consisting of a self-stabilizing mechanism. If blowup conditions develop the slide accelerates as
853 much as a planar slide. However, the creeping stage is also controlled, in addition to aspects
854 valid for planar slides, by geometrical details and the evolutionary changes in slide geometry.

855 Finally, although the intention of the paper was to provide a theoretical investigation of the
856 problem rather than an analysis of a specific landslide, the models presented can be readily
857 used on appropriate real cases, at least as a back-analysis tool. Predictive modelling is also
858 possible in principle; however a pertinent issue in this respect is the calibration of material
859 parameters, especially the rate parameter, which may have significant impact on predictions.

860

861 REFERENCES
862
863

864 Alcántara-Ayala, I. & Domínguez-Morales, L. (2008). The San Juan de Grijalva catastrophic
865 landslide, Chiapas, Mexico: lessons learnt. *Web Proceedings of the First World Landslide*
866 *Forum.* International Consortium on Landslides. United Nations International Strategy for
867 Disaster Reductions. Nicola Casagli, Riccardo Fanti, Veronica Tofani (eds.). Tokyo, Japan, 96-
868 99.

869 Alonso, E. E., & Pinyol, N. M. (2014). Slope stability in slightly fissured claystones and marls.
870 *Landslides*. Published online.

871 Alonso, E., Pinyol, N. & Puzrin, A. (2010). *Geomechanics of Failures. Advanced Topics*, Springer.

872 Alonso, E.E., Pinyol, NM & Yerro, A (2014). Mathematical Modelling of Slopes. *Procedia Earth*
873 *and Planetary Science* **9**, 64–73.

874 Campbell, C.S., Cleary, P.W. & Hopkins, M.A. (1995). Large-scale landslide simulations: global
875 deformation, velocities, and basal friction. *J. Geophys. Res. Solid. Earth* **100**, No. B5, 8267–
876 8283.

877 Andersen, S. & Andersen, L. (2010). Modelling of landslides with the material-point method.
878 *Computational Geosciences* **14**, No. 1, 137–147.

879 Bardenhagen, S.G. & Kober, E.M. (2004). The generalized interpolation material point method.
880 *Computer Modeling in Engineering and Sciences* **5**, No. 6, 477–495.

881 Bishop A. W. (1971). The influence of progressive failure on the choice of the method of
882 stability analysis. *Géotechnique* **21**, 168–172.

883 Bishop, A. W. (1967). Progressive failure-with special reference to the mechanism causing it.
884 *Proceedings of the Geotechnical Conference*, *Olso*, Vol. 2, 142–150.

885 Bjerrum L (1967). Progressive failure in slopes of overconsolidated plastic clay and clay- shales.
886 *J. Soil. Mech. Fdn. Div. Am. Soc. Civ. Eng.* **93**, No. SM5, 3–49.

887 Bowden, F. & Tabor, D (1964). *The friction and lubrication of solids*. New York. Oxford
888 University Press.
889 Cascini, L., Cuomo, S., Pastor, M., & Sorbino, G. (2010). Modeling of Rainfall-Induced Shallow
890 Landslides of the Flow-Type. *Journal of Geotechnical and Geoenvironmental Engineering* **1**
891 No. January, 85–98.
892 Cecinato, F. & Zervos, A. (2012). Influence of thermomechanics in the catastrophic collapse of
893 planar landslides. *Canadian Geotechnical Journal* **49**, No. 2, 207–225.
894 Cecinato, F., Zervos, A. & Veveakis, E. (2011). A thermo-mechanical model for the catastrophic
895 collapse of large landslides. *Int. J. Numer. Anal. Meth. Geomech.* **35**, 1507-1535.
896 Chamot, P. (1993). El deslizamiento La Josefina en el Valle del Tío Paute. Report to the United
897 Nations, 16p.
898 Chen, T. C., Lin, M. L., & Hung, J. J. (2003). Pseudostatic analysis of Tsao-Ling rockslide caused
899 by Chi-Chi earthquake. *Engineering Geology* **71**, No.1-2, 31–47.
900 Cleary, P. W. & C. S. Campbell (1993). Self-lubrication for Long Runout Landslides: Examination
901 by computer simulation. *J. Geophys. Res*. **98**, No. B12, 21911–21924.
902 Conte, E., Silvestri, F. & Troncone, A. (2010). Stability analysis of slopes in soils with strain-
903 softening behaviour. *Computers and Geotechnics* **37**, No. 5, 710–722.
904 Cooper, M. (1996). The progressive development of a failure slip surface in over-consolidated
905 clay at Selborne, UK. *7th Int. Symp. on Landslides.* Trondheim, Norway. Senneset, K. (ed.),
906 Balkema, 683–688.
907 Cooper, M.R., Bromhead, E.N., Petley, D.J. & Grant, D.I. (1998). The Selbourne cutting stability
908 experiment. *Géotechnique* **48**, No. 1, 83–101.
909 Dai, F.C, Deng, J.H., Tham, L.G., Law, K.T. & Lee, C.F. (2004). A large landslide in Zigui County,
910 Three Gorges area. *Canadian Geotechnical Journal* **41**, 1233-1240.
911 Darve, F. & Laouafa, F. (2000). Instabilities in granular materials and application to landslides.
912 *Mech. Cohes.-Frict. Mater.* **5**, 627–652.

913 Davis R.O., Desai, C.S. & Smith, N.R. (1993). Stabiltiy of motions of translatinoal landslide.
914 *Journal of Geotechnical Engineering* **119**, No. 3, 420-432.
915 De Blasio, F. V. (2008). Production of frictional heat and hot vapour in a model of self-
916 lubricating landslides. *Rock Mechanics and Rock Engineering* **41**, 219–226.
917 Di Toro, G., Hirose, T., Nielsen, S., Pennacchioni, G., & Shimamoto, T. (2006). Natural and
918 experimental evidence of melt lubrication of faults during earthquakes. *Science* **311**, No.
919 February, 647–649.
920 Dieterich, J. (1979) Modeling of rock friction 1. Experimental results and constitutive
921 equations. *Journal of Geophysical Research* **84**, No. B5, 2161-2168.
922 Dounias GT, Potts DM and Vaughan PR (1996). Analysis of progressive failure and cracking in
923 old British dams. *Géotechnique* **46**, No. 4, 621–640.
924 Dowell, M. & Jarratt, P. (1972). The "Pegasus" method for computing the root of an equation.
925 *BIT* **12**, 503-508.
926 Duncan, J. (1996). State of the Art: Limit Equilibrium and Finite-Element Analysis of Slopes. *J.*
927 *Geotech. Engrg.* **122**, No. 7, 577–596.
928 Ferri, F., Di Toro, G., Hirose, T., & Shimamoto, T. (2010). Evidence of thermal pressurization in
929 high-velocity friction experiments on smectite-rich gouges. *Terra Nova* **22**, No. 5, 347–353.
930 Follacci, J.-P., L. Rochet & J.-F. Serratrice (1993). Glissement de La Clapière, St. Etienne de
931 Tinée, Synthèse des connaissances et actualisation des risques,
932 rapp.92/PP/UN/I/DRM/03/AI/01, 76 pp., Cent. Etud. Tech. de l'Equip., Nice, France.
933 Gens, A. & Alonso, E.E. (2006). Aznalcóllar dam failure. Part 2: Stability conditions and failure
934 mechanism. *Géotechnique* **56**, No. 3, 185–201.
935 Goguel, J. (1978) Scale-dependent rockslide mechanisms, with emphasis on the role of pore
936 fluid vaporization. *Rockslides and avalanches.* Voight, B. (ed.) Elsevier, Amsterdam, 693–
937 706.

938 Goren, L. & Aharonov, E. (2007). Long runout landslides: The role of frictional heating and
939 hydraulic diffusivity. *Geophysical Research Letters* **34**, No. L07301, 1–7.
940 Goren, L. & Aharonov, E. (2009). On the stability of landslides: A thermo-poro-elastic approach.
941 *Earth and Planetary Science Letters* **277**, No. 3-4, 365–372.
942 Goren, L. & Aharonov, E. (2009). On the stability of landslides: A thermo-poro-elastic approach.
943 Earth and Planetary Science Letters, 277(3-4), 365–372.
944 Goren, L., Aharonov, E. & Anders, M. H. (2010). The long runout of the Heart Mountain
945 landslide: Heating, pressurization, and carbonate decomposition. *Journal of Geophysical*
946 *Research: Solid Earth* **115**, No. B10, 1–15.
947 Habib, P. (1975) Production of gaseous pore pressure during rock slides. *Rock. Mech. Rock.*
948 *Engng*. **7**, 193–197.
949 Han, R., & Hirose, T. (2012). Clay-clast aggregates in fault gouge: An unequivocal indicator of
950 seismic faulting at shallow depths?. *Journal of Structural Geology* **43**, No. October, 92–99.
951 Harden, C.P. (2004). The 1993 Landslide dam at La Josefina in Southern Ecuador: A review of
952 “Sin plazo para La Esperanza”. *Engineering Geology* **74**, No. 1-2, 157-161.
953 He, S.-M., Liu, W. & Wang, J. (2015). Dynamic simulation of landslide based on thermo-poro-
954 elastic approach. *Computers & Geosciences* **75**, No. February, 24–32.
955 Helmstetter A., Sornette D., Grasso J. R., Andersen J. V., Gluzman S &, Pisarenko, V. (2003)
956 Slider-block friction model for landslides: application to Vajont and La Clapière landslides. *J.*
957 *Geophys. Res*. **109**, No. B02409.
958 Hendron, A.J. & Patton, F.D. (1985). The Vaiont slide, a geotechnical analysis based on new
959 geologic observations of the failure surface. *Technical Report GL–85–5*. Department of the
960 US Army Corps of Engineers, Washington, DC.
961 Hewitt, K., Clague, J. J., & Orwin, J. F. (2008) Legacies of catastrophic rock slope failures in
962 mountain landscapes. *Earth-Science Reviews* **87** (2008), 1–38.

963 HSL. A collection of Fortran codes for large scale scientific computation.
964 http://www.hsl.rl.ac.uk/
965 HSL. A collection of Fortran codes for large scale scientific computation.
966 http://www.hsl.rl.ac.uk/ (accessed February 2015).
967 Hungr, O., Leroueil, S. & Picarelli, L. (2014). The Varnes classification of landslide types, an
968 update. *Landslides* **11**, 167–194.
969 IUGS - International working group, L. (1995). A suggested method for describing the rate of
970 movement of a landslide. *Bulletin of the International Association of Engineering Geology*
971 **52**, 75-78.
972 Iverson, R. M., Reid, M. E. & Lahusen, R. G. (1997). Debris-flow mobilization from landslides.
973 *Annu. Rev. Earth Planet Sci.* **25**, 85–138.
974 Leroueil, S. (2001). Natural slopes and cuts: movement and failure mechanisms. *Géotechnique*
975 **51**, No. 3, 197-243.
976 Liao, C. J., Lee, D. H., Wu, J. H., & Lai, C. Z. (2011). A new ring-shear device for testing rocks
977 under high normal stress and dynamic conditions. *Engineering Geology* **122**, No. 1-2, 93–
978 105.
979 Mesri, G., and Shahien, M. (2003). Residual shear strength mobilized in first-time slope
980 failures. *J. Geotech. Geoenviron. Eng.* **129**, No. 1, 12-31.
981 Mitchell, J.K. 1976. *Fundamentals of soil behaviour.* New York. John Wiley & Sons.
982 Mizoguchi, K., Hirose, T., Shimamoto, T., & Fukuyama, E. (2007) Reconstruction of seismic
983 faulting by high-velocity friction experiments: An example of the 1995 Kobe earthquake.
984 *Geophysical Research Letters* **34**, No. August, 2–4.
985 Müller, L. (1964). The rock slide in the Vajont Valley. *Rock Mechanics and Engineering Geology*
986 **2**, 148–212.
987 Nonveiller, E. (1987). The Vajont reservoir slope failure. *Engineering Geology* **24**, 493–512.

988 Paronuzzi, P., Rigo, E. & Bolla, A. (2013). Influence of filling–drawdown cycles of the Vajont
989 reservoir on Mt. Toc slope stability. *Geomorphology* 191, 75–93.
990 Pastor, M., Blanc, T., Haddad, B., Drempetic, V., Morles, M. S., Dutto, P., Stickle, M.M, Mira, P.
991 & Merodo, J. A. (2014). Depth Averaged Models for Fast Landslide Propagation:
992 Mathematical, Rheological and Numerical Aspects. *Archives of Computational Methods in*
993 *Engineering* **22**, No. 1, 67–104.
994 Pinyol, N. M. & Alonso, E. E. (2010a). Criteria for rapid sliding II. *Engineering Geology* **114**, No.
995 3-4, 211–227.
996 Pinyol, N. M. & Alonso, E. E. (2010b). Fast planar slides. A closed-form thermo-hydro-
997 mechanical solution. *Int. J. Numer. Anal. Meth. Geomech.* **34**, 27–52.
998 Pinyol, N. M., Alonso, E. E., Corominas, J. & Moya, J. (2011). Canelles landslide: modelling rapid
999 drawdown and fast potential sliding. *Landslides* **9**, No. 1, 33–51.
1000 Plaza-Netos, G. and Zevallos, O. (1994) The La Josefina rockslide. In The 1993 La Josefina
1001 Rockslide and Río Paute Landslide Dam. Ecuador. *Landslides News* **8**, 4-6.
1002 Potts, D.M., Dounias, G.T. & Vaughan, P.R. (1990). Finite element analysis of progressive failure
1003 of Carsington embankment. *Géotechnique* **40**, No. 1, 79–101.
1004 Rice, J. R. (2001). New perspectives in crack and fault dynamics. Mechanics for a New
1005 Millennium. *Proc. of the 20th Int. Congress of Theoretical and Applied Mechanics*. H. Aref
1006 and J. W. Phillips (eds.). Chicago. Kluwer Academic Publishers, 1-23.
1007 Rice, J. R., Lapusta, N. & Ranjith, K. (2001). Rate and state dependent friction and the stability
1008 of sliding between elastically deformable solids. *Journal of the Mechanics and Physics of*
1009 *Solids* **49**, 1865-1898.
1010 Ruina, A. (1983). Slip instability and state variable friction laws. *J. Geophys. Res.* **8**, No. B12,
1011 10359-10370.
1012 Saito M (1965). Forecasting the time of occurrence of a slope failure. *Proc. 6th Int. Conference*
1013 *on Soil Mechanics and Foundation Engineering. Montreal.* Vol. 2, 315–318.

1014 Saito, M. (1969). Forecasting time of slope failure by tertiary creep*. Proc. 7th International*
1015 *Conference on Soil Mechanics and Foundation Engineering. Mexico City.* Vol. 2*,* 677–683*.*
1016 Schuster, R.L., Salcedo, D.A. and Valenzuela, L. (2002). Overview of catastrophic landslides of
1017 South America in the twentieth century. *Catastrophic Landslides: Effects, Occurrences and*
1018 *Mechanism.* Evans, S.G. and DeGraff, J.V. (eds.). Geological Society of America.
1019 Semenza, E. (2001). La Storia del Vaiont Raccontata del Geologo che ha Scoperto la Frana.
1020 *Tecomproject*. Editore Multimediale. Ferrara.
1021 Skeel, R. D. (1986). Construction of variable-stepsize multistep formulas. *Mathematics of*
1022 *Computation* **47**, No. 176, October, 503-510.
1023 Skempton A.W., Petley, F.R.S and Petley, D.J. (1967). The strength along structural
1024 discontinuities in stiff clays. *Proc. of Geotechnical Conference*. *Olso, Norwegian*. Vol. 2, 55-
1025 69.
1026 Skempton, A. W. (1985). Residual Strength of Clays in Landslides, Folded Strata, and the
1027 Laboratory. *Géotechnique* **35**, No. 1, 3-18.
1028 Sosio, R., Crosta, G. B., & Hungr, O. (2008). Complete dynamic modeling calibration for the
1029 Thurwieser rock avalanche (Italian Central Alps). *Engineering Geology* **100**, 11–26.
1030 Tang, C. L., Hu, J. C., Lin, M. L., Angelier, J., Lu, C. Y., Chan, Y. C., & Chu, H. T. (2009). The
1031 Tsaoling landslide triggered by the Chi-Chi earthquake, Taiwan: Insights from a discrete
1032 element simulation. *Engineering Geology* **106** , No. 1-2, 1–19.
1033 Tika, T. E., Vaughan, P. R. & Lemos, L. (1996). Fast Shearing of Pre-Existing Shear Zones in Soil.
1034 Géotechnique **46**, No. 2, 197-233.
1035 Ujiie, K., & Tsutsumi, A. (2010). High-velocity frictional properties of clay-rich fault gouge in a
1036 megasplay fault zone, Nankai subduction zone. *Geophysical Research Letters* **37**, No.
1037 December, 1–5.

1038 Uriel Romero, S. & Molina, R. (1977). Kinematic aspects of Vaiont slide. *Proc. of the 3rd*
1039 *International Conference of the ISRMR. Denver, USA*. National Academy of Sciences 2B,
1040 865–870.
1041 Vardoulakis, I. (2000). Catastrophic landslides due to frictional heating of the failure plane.
1042 *Mechanics of Cohesive-frictional Materials* **5**, No. 6, 443–467.
1043 Vardoulakis, I. (2002). Dynamic thermo-poro-mechanical analysis of catastrofic landslides.
1044 *Géotechnique* **52**, No. 3, 157–171.
1045 Veveakis, E., Vardoulakis, I. & Di Toro, G. (2007). Thermoporomechanics of creeping landslides:
1046 The 1963 Vaiont slide, northern Italy. *Journal of Geophysical Research* **112**, No. F3, F03026.
1047 Voight, B. (1978) *Rockslides and avalanches*, Volume 1, New York, Elsevier.
1048 Voigt, B. & Faust, C. (1982). Frictional heat and strength loss in some rapid landslides.
1049 *Géotechnique* **32**, No. 1, 43–54.
1050 Wagner, W. & Kruse, A. (1998). *Properties of Water and Steam.* Springer-Verlag
1051 Wang, F.W., Zhang, Y.M., Huo, A.T., Matsumoto, T. & Huang, B.T. (2004) The July 14, 2003
1052 Qianjiangping landslide, Three Gorges Reservoir, China. *Landslides* **1**, 157-162.
1053 Wedage, A., Morgenstern, N. R. & Chan, D. H. (1998). A strain rate dependent constitutive
1054 model for clays at residual strength. *Canadian Geotechnical Journal* **35**, 364–373.
1055 Więckowski, Z., Sung-Kie, Y. & Jeoung-Heum, Y. (1999). A particle-in-cell solution to the silo
1056 discharging problem. *Int. J. Numer. Anal. Meth. Geomech.* **45**, No. 9, 1203–1225.
1057 Wu, J-H. & Chen, C-H (2011). Application of DDA to simulate characteristics of the Tsaoling
1058 landslide. *Computers and Geotechnics* **38**, No. July, 741–750.
1059 Yang, C-M., Yu, W-L., Dong, J-J., Kuo, C-Y., Shimamoto T., Lee, C-T., Togo, T., Miyamoto, Y.
1060 (2014). Initiation, movement, and run-out of the giant Tsaoling landslide — What can we
1061 learn from a simple rigid block model and a velocity–displacement dependent friction law?.
1062 *Engineering Geology* **182** Part B, No. November, 158–181.

1063 Yerro, A., Alonso, E.E & Pinyol, N.M. (2014). Modelling progressive failure with MPM.
1064 *Numerical Methods in Geotechnical Engineering* NUMGE 2014, Delf. Hicks M, Brinkgreve
1065 RBJ and Rohe A (eds.). Balkema, Leiden, The Netherlands, Vol. 1, 319–323.
1066 Zabala, F. & E.E. Alonso (2011). Progressive failure of Aznalcóllar dam using the Material Point
1067 Method. *Géotechnique* **61**, No. 9, 795–808.
1068

1069 FIGURES

1070

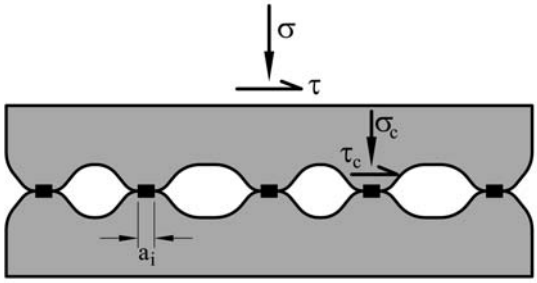

1071
1072
1073 Figure 1. Sketch to illustrate the concept of friction.
1074

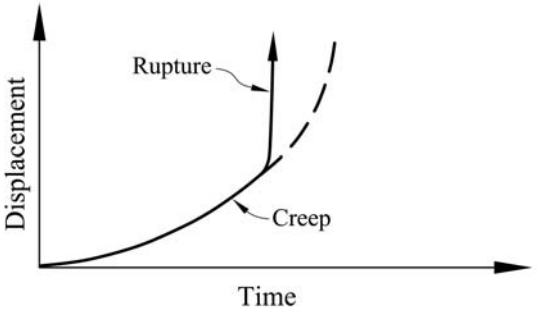

1075

1076

1077 Figure 2. Creep and rupture: two interacting mechanisms in action
1078

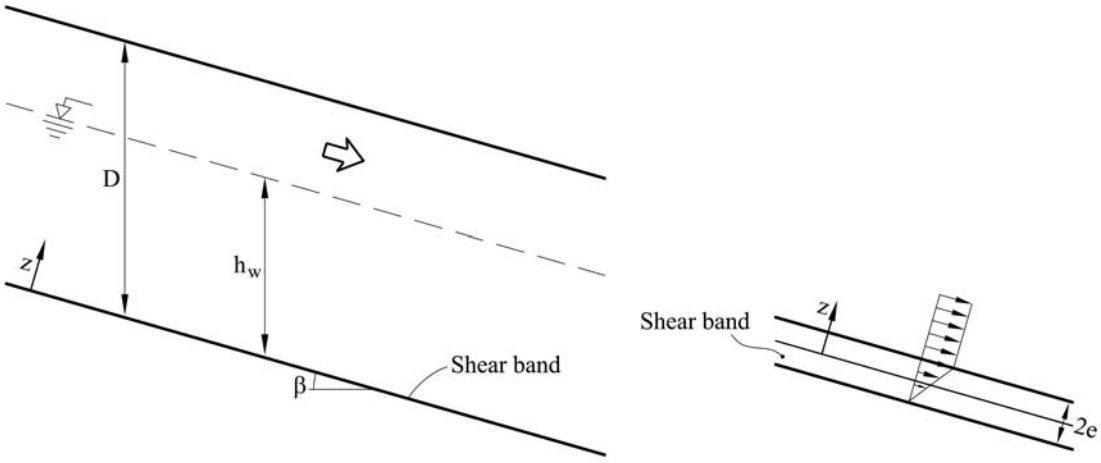

1079

1080 Figure 3. Geometry of a planar landslide and shear band

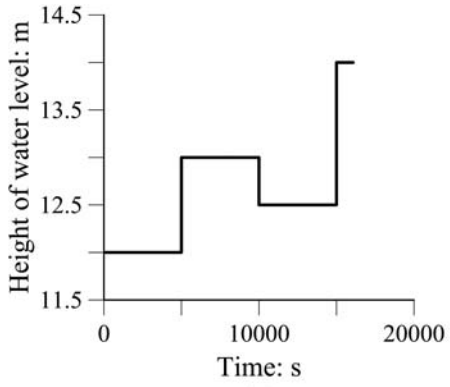
Height of water level: m
14.5
13.5
12.5
11.5
0
10000
20000
Time: s

(a)

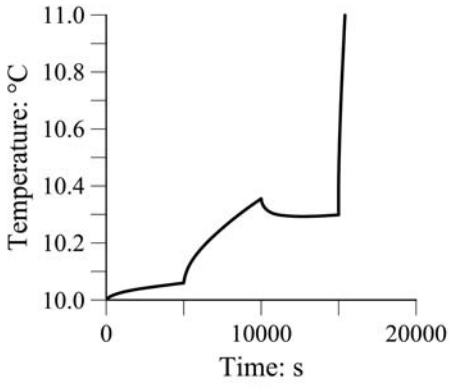
Temperature: °C
11.0
10.8
10.6
10.4
10.2
10.0
0
10000
20000
Time: s

(b)

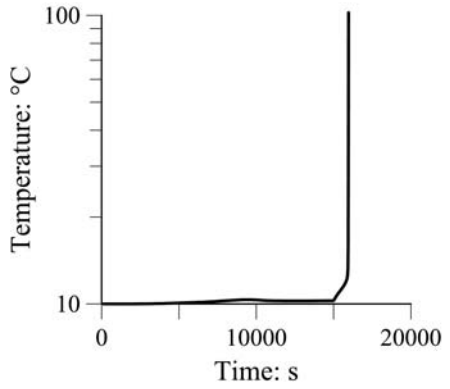
Temperature: °C
100
10
0
10000
20000
Time: s

(c)

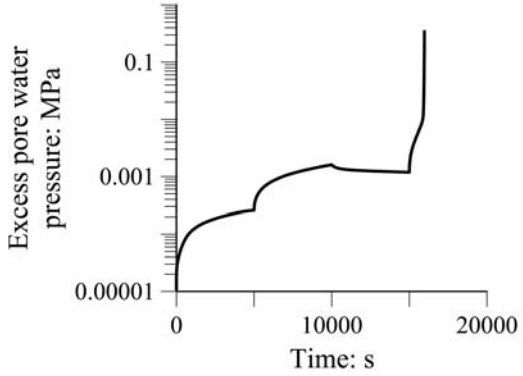
Excess pore water pressure: MPa
0.1
0.001
0.00001
0
10000
20000
Time: s

(d)

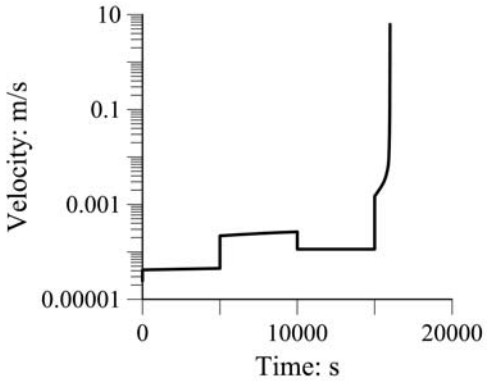
Velocity: m/s
10
0.1
0.001
0.00001
0
10000
20000
Time: s

(e)

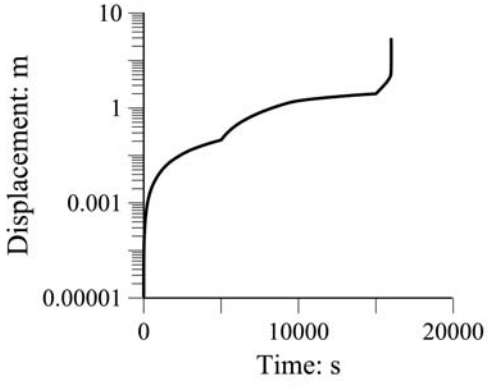
Displacement: m
10
1
0.001
0.00001
0
10000
20000
Time: s

(f)

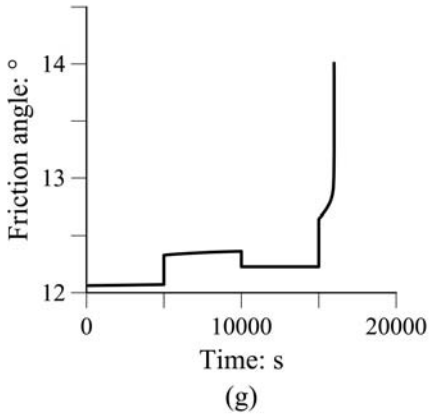

1081 Figure 4. Calculated response of an impending planar slide to an imposed variation of water level (a). (b),
1082 (c): Temperature at the center of shear band; (d): Excess pore water pressure at the center of shear
1083 band; (e): slide velocity; (f): slide displacement; (g): evolution of friction angle.

1084

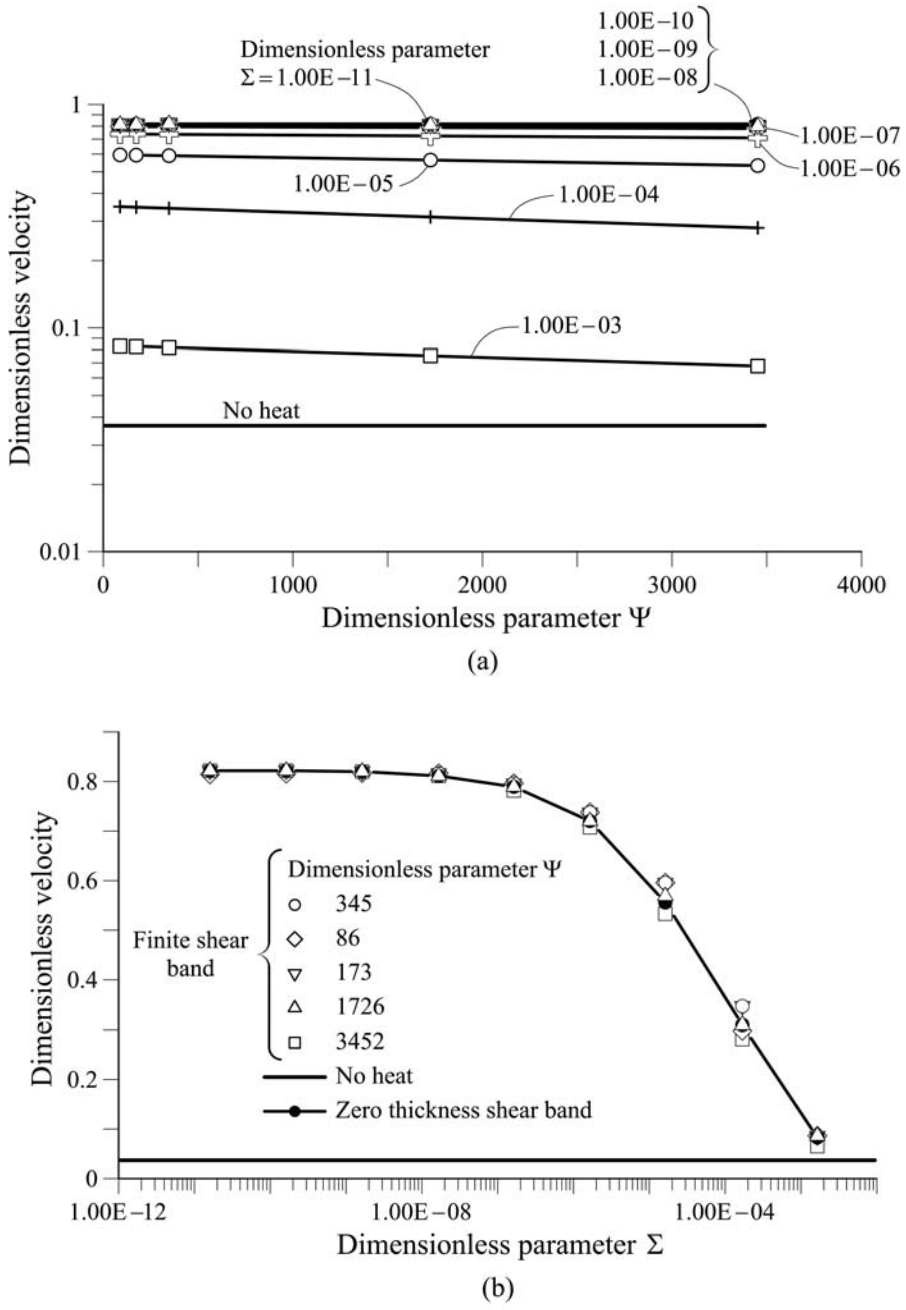

Figure 5. Dimensionless velocity reached at a displacement equal to twice the height of the sliding mass for different values of two dimensionless parameters: parameters Ψ (coefficient of heat source term in the energy balance equation) and Σ, (coefficient of consolidation in the mass balance equation of water flow). Π (coefficient of rate of temperature in the mass balance equation) is equal to 1. Rate independent friction.

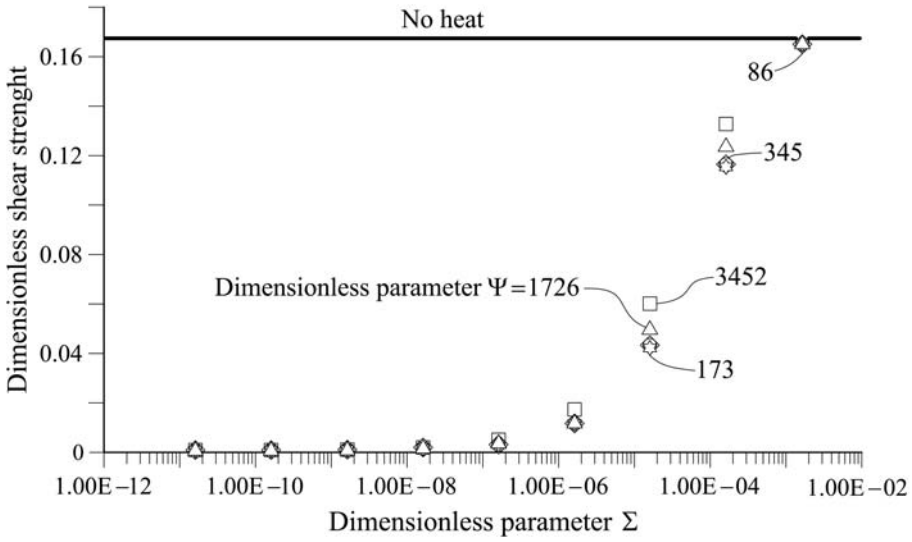

1093

1094 Figure 6. Ratio of final and initial shear strength for different values of two dimensionless parameters:
1095 parameter Ψ (coefficient of heat source term in the energy balance equation) and Σ (coefficient of
1096 consolidation in the mass balance equation of water flow). Π (coefficient of rate of temperature change
1097 in the mass balance equation) is equal to 1. Rate independent friction.

1098

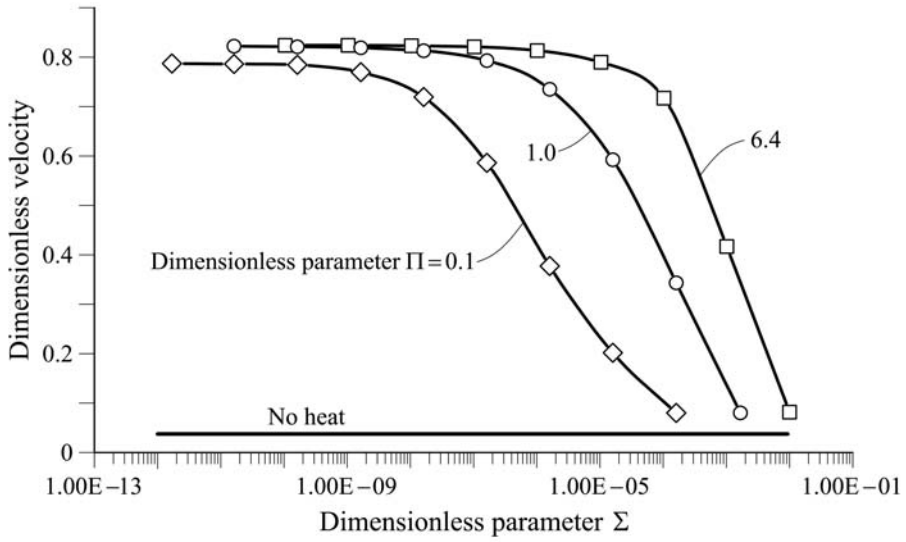

1099

1100 Figure 7. Dimensionless velocity reached at 50 m of displacement for different values of two
1101 dimensionless parameters: parameter Π (coefficient of rate of temperature change in the mass balance
1102 equation) and Σ (coefficient of consolidation in the mass balance equation of water flow). Ψ, the
1103 coefficient of heat in the energy balance equation, is equal to 345. Rate independent friction.

1104

1105

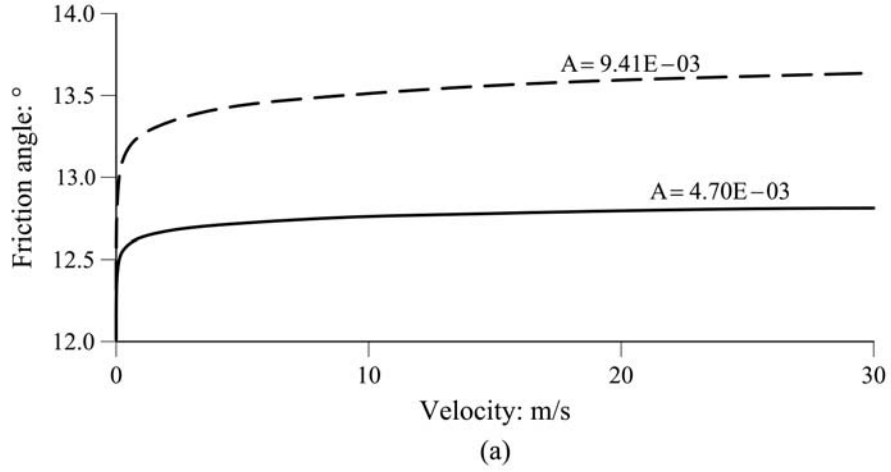

1106

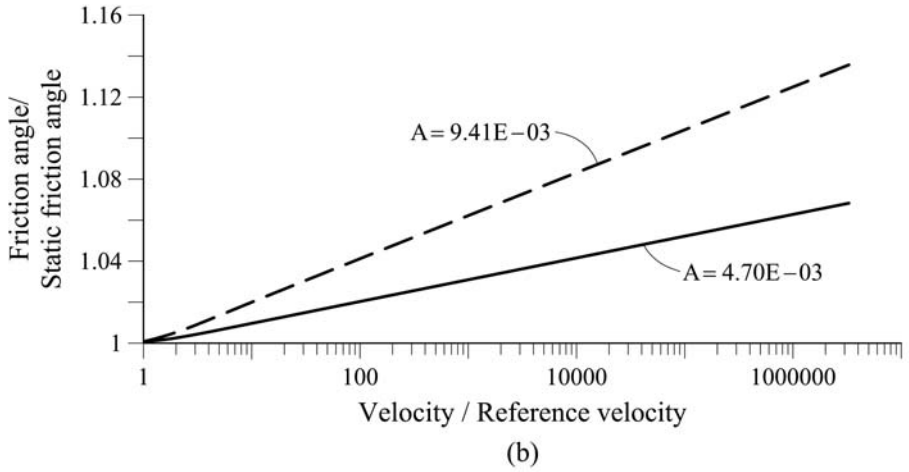

1107

1108 Figure 8. Friction angle as a function of shearing velocity for two different *A* parameters. (a) Friction
1109 angle vs velocity; (b) Ratio between friction angle and static friction angle associated with log velocity
1110 values lower than a reference vel ($\hat{v}_{ref} = 6.4 \cdot 10^{-7}$).

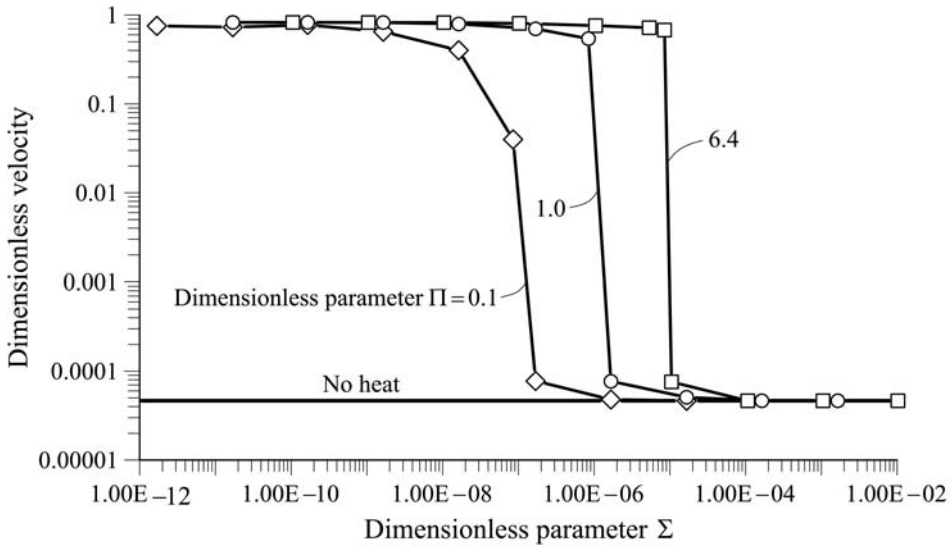

1111

Figure 9. Dimensionless maximum velocity in terms of dimensionless parameters Π (coefficient of rate of temperature change in the mass balance equation) and Σ (coefficient of consolidation in the mass balance equation of water flow). Ψ (coefficient of heat source term in the energy balance equation) is equal to 345. Rate dependent friction parameters: A=4.7·10^{-3} and $\hat{v}_{ref} = 6.4 \cdot 10^{-7}$.

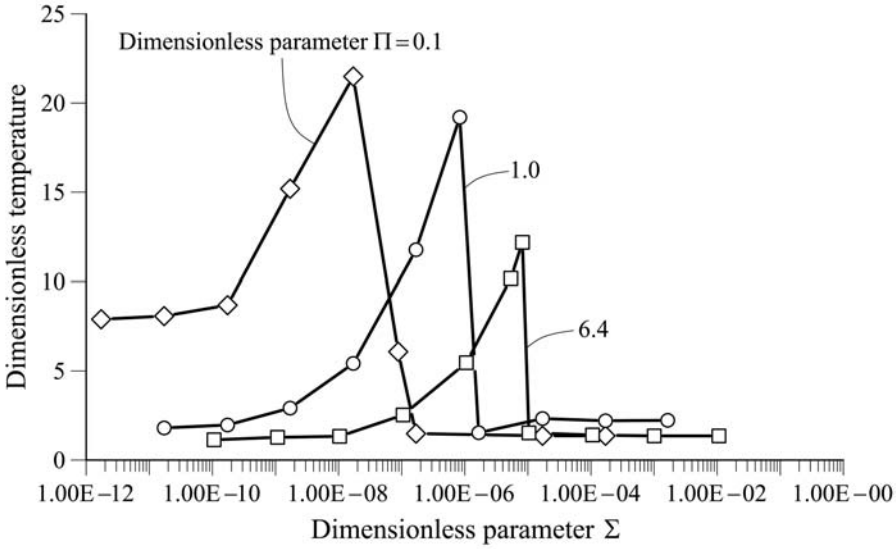

Figure 10. Dimensionless temperature for different dimensionless parameters: parameter Π (coefficient of rate of temperature change in the mass balance equation) and Σ (coefficient of consolidation in the mass balance equation of water flow). Ψ (coefficient of heat source term in the energy balance equation) is equal to 345. Rate dependent friction with A=4.7·10^{-3} and a reference velocity equal to $\hat{v}_{ref} = 6.4 \cdot 10^{-7}$.

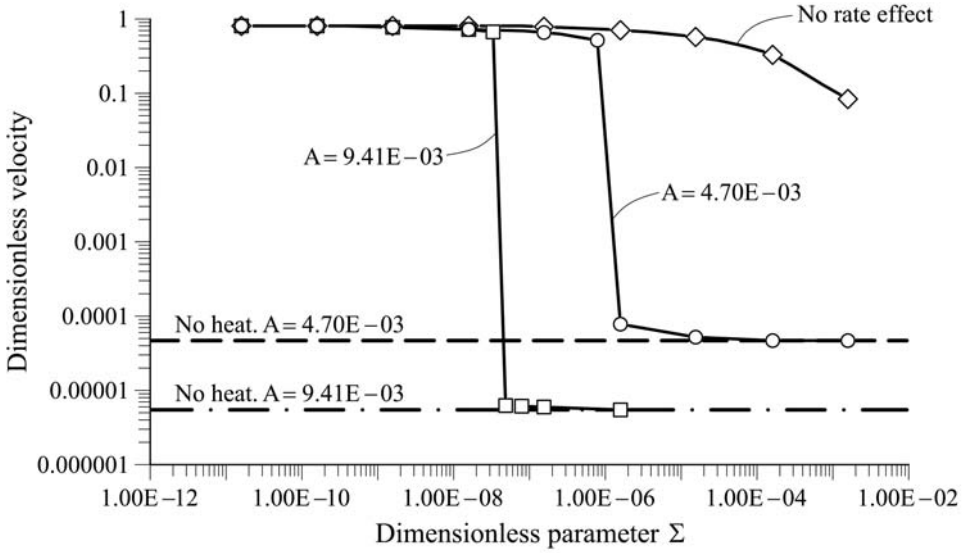

Figure 11. Dimensionless velocity in terms of dimensionless parameters Π (coefficient of rate of temperature change in the mass balance equation) and Σ (coefficient of consolidation in the mass balance equation of water flow) for three values of the rate effect parameter A. Ψ (coefficient of heat source term in the energy balance equation) is equal to 345. In all cases plotted, v_{ref} = 10^{-5} m/s.

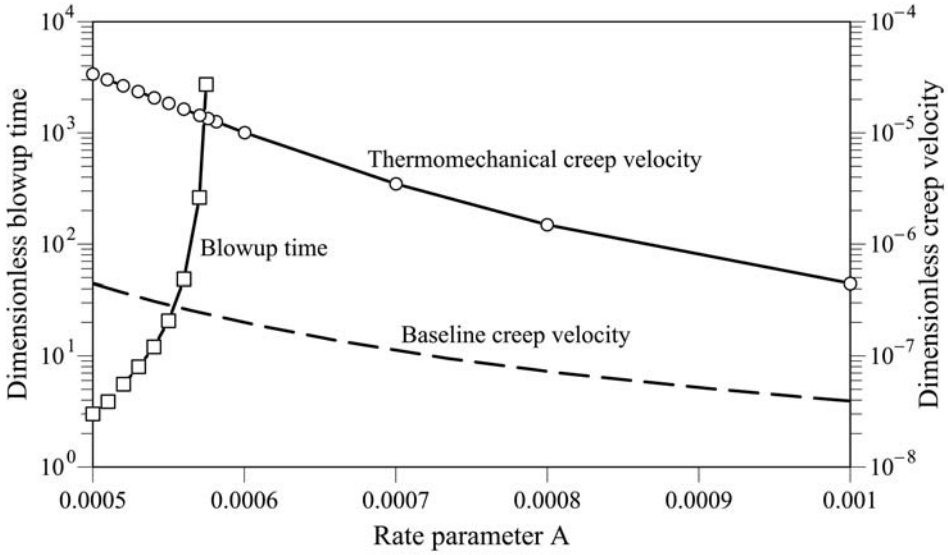

1128

1129 Figure 12. Effect of rate parameter on creep velocity and blowup time

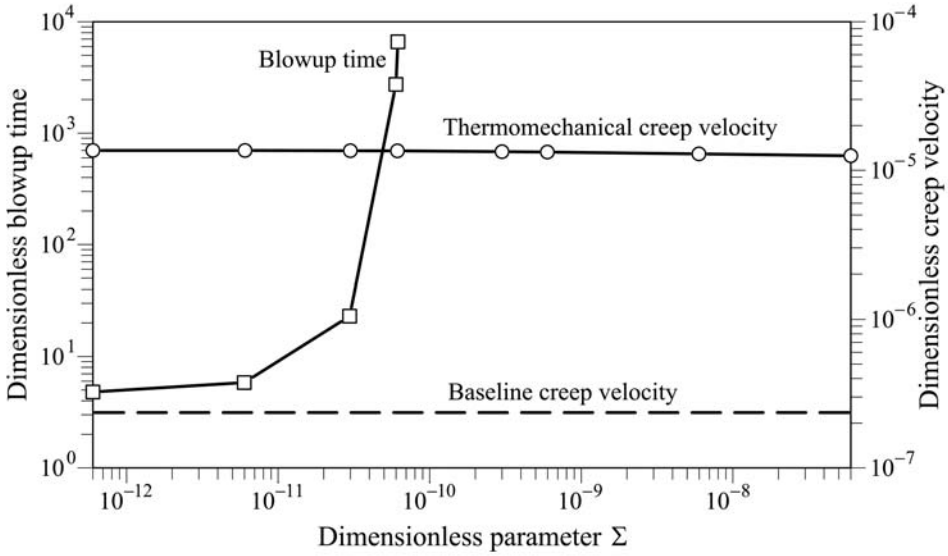

1130

1131 Figure 13. Effect of the dimensionless parameter Σ (coefficient of consolidation in the mass

1132 balance equation of water flow) on creep velocity and blowup time

1133

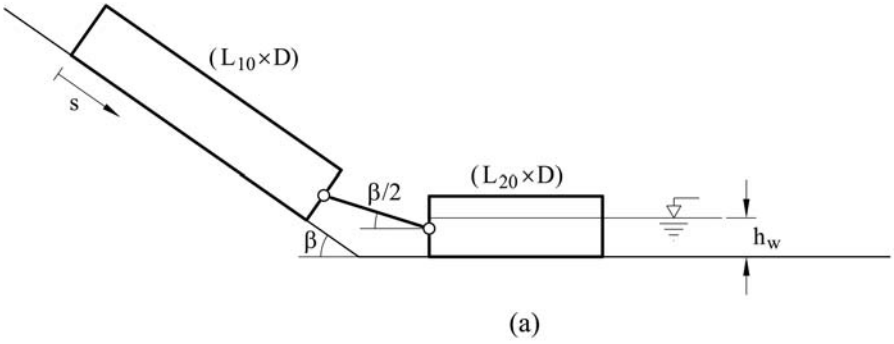

1134

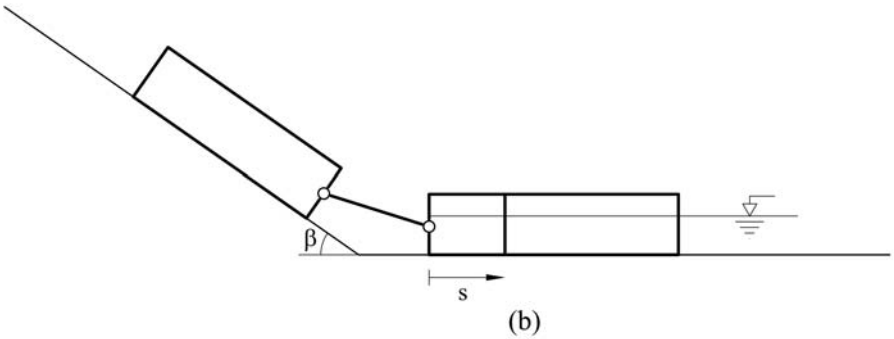

1135

1136 Figure 14. The two-block model analysed.

1137

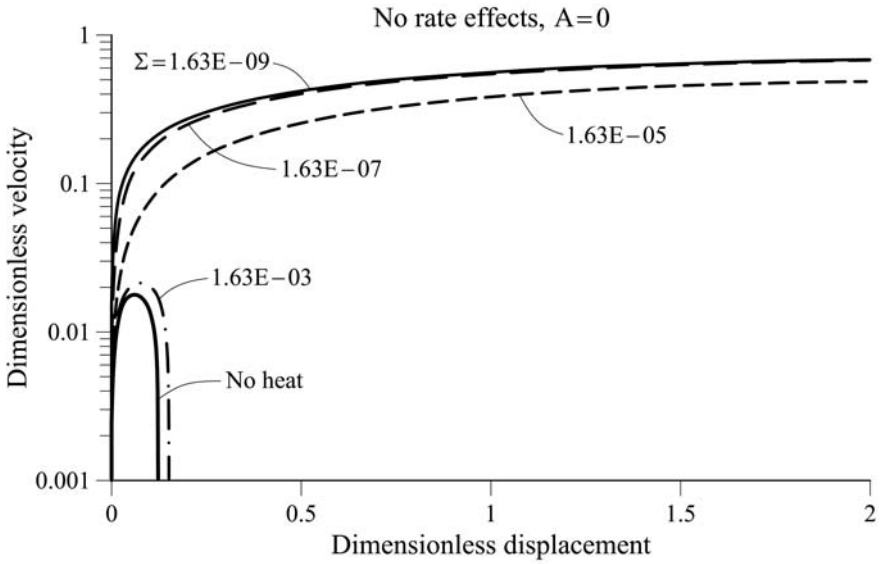

Figure 15. Thermal analysis of two block model; no rate effect on friction (*A*=0). Effect of dimensionless parameter Σ (coefficient of consolidation in the mass balance equation of water flow) on velocity and run-out.

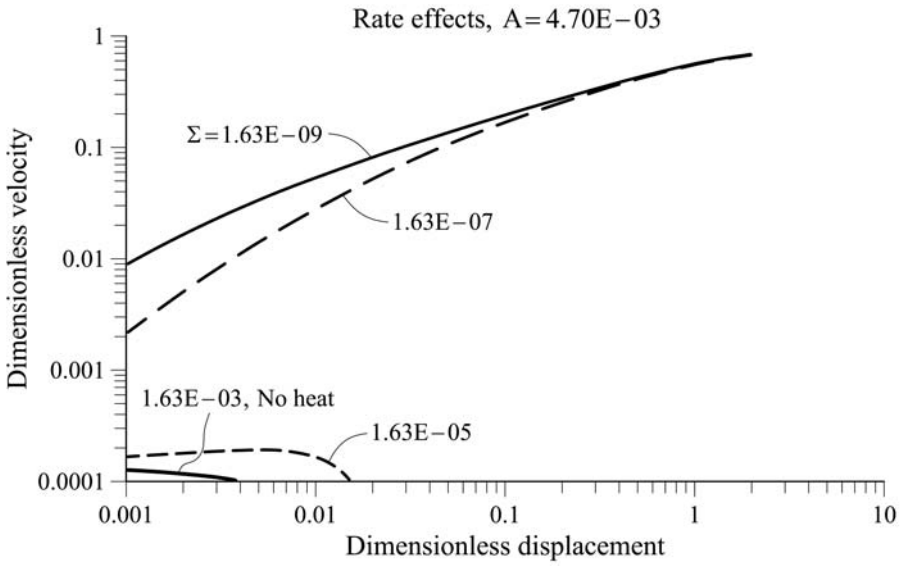

1147

1148 Figure 16. Thermal analysis of two block model; rate effect on friction characterized by

1149 A=4,7·10^{-3} and a reference velocity equal to $\hat{v}_{ref} = 6.4 \cdot 10^{-7}$. Effect of band permeability on

1150 velocity and run-out.

1151

TABLE

Table 1. Contributions to thermal analysis of catastrophic landslides

References	**Problem description and governing equations**	**Sliding geometry**	**Constitutive modelling**	**Case analyzed and particular characteristics**	**Main emphasis**
Habib (1967)	Heat induced by friction on a shear band, including heat losses.	Planar	N/A		Generated vapour pressure in the shearing band may explain a rapid motion
Romero and Molina (1974)	Dynamics of motion expressed as a balance of energy: slide deformation, basal friction, impulse of reservoir water and kinetic energy. Pore pressure determined in a phase diagram vapour-liquid water	Compound failure surface. Defined by vertical slices	Mohr-Coulomb	Vaiont. Run-out and velocity determined during the entire motion	Explaining the high velocity of Vaiont
Voigt and Faust (1982)	Rigid mass sliding and deformation concentration in a shear band Saturated shear band Terzaghi's effective stress Mass, energy and momentum balances One dimensional model for heat and pore water pressure dissipation.	Planar	Mohr-Coulomb	Vaiont. Average block. 1D Finite Element analysis	Heat induced fluid pressure explains Vaiont velocity
Vardoulakis (2000, 2002)	As in V&F(1982)	Slip circle	Mohr-Coulomb frictional strength	Vaiont.	Dynamic post failure response

	Numerical analysis Heat advective term negligible No vapour generation		Shear strain and shear strain rate softening of frictional coefficient Thermal expansion coefficient of the soil skeleton including thermoelastic expansion and thermoplastic collapse	Slide triggering by reducing the frictional angle from the strict equilibrium	
Veveakis et al. (2007)	As in V&F(1982) Analytical solutions	Planar	Mohr-Coulomb frictional strength Thermal softening and velocity strengthening law for frictional coefficient Thermal expansion coefficient of the soil skeleton including thermoelastic expansion and thermoplastic collapse	Vaiont. Slide triggering by reducing frictional angle from strict equilibrium Constant water table in Veveakis et al. (2007)	Long creeping phase of Vaiont landslide and the final high acceleration due to the onset of thermal pressurization
Goren & Aharonov (2007)	As in V&F(1982) Numerical analysis Advective term and heat conduction negligible No vapour generation	Planar	Mohr-Coulomb frictional strength Constant frictional coefficient	Synthetic cases Slide triggering by an initial velocity Sensitivity analysis	Long travel distances of landslides and their relation to slide volumes depending on the depth dependent permeability
Goren & Aharonov (2009)	As in V&F(1982) Numerical analysis Advective term and heat conduction negligible No vapour generation	Planar	Mohr-Coulomb frictional strength Constant frictional coefficient Constant thermal expansion coefficient	Synthetic cases Slide triggering by imposing an initial velocity (e.g. simulating an earthquake) and imposing an excess pore	Sensitivity analysis of the triggering factors and constitutive and geometrical parameters to evaluate the effect on the regime of the

				water pressure that dissipates in time (e.g. simulating rain of snow melt infiltration).	landslide which may become an arrested or catastrophic slide.
Pinyol and Alonso (2010a)	As in V&F(1982) Analytical solution Advective term and heat conduction negligible Incompressible water and soil skeleton No vapour generation	Planar	Mohr-Coulomb frictional strength Constant frictional coefficient Constant thermal expansion coefficient	Synthetic cases Slide triggering by increasing the water level	Analytical solution for the slide velocity. Sensitivity analysis of constitutive and geometrical parameters to evaluate the slide evolution.
Pinyol and Alonso (2010b)	As in V&F(1982) Numerical analysis Advective term and heat conduction negligible No vapour generation	Compound failure surface. Two interacting wedges describe evolving geometry	Mohr-Coulomb frictional strength Constant frictional coefficient Constant thermal expansion coefficient	Vaoint. Slide triggering by increasing the water reservoir level from the strict equilibrium	Dynamic post failure response. Sensitivity analysis of constitutive parameters and scale effects.
Goren et al (2010)	As in V&F(1982) Numerical analysis Advective term and heat conduction negligible No vapour generation	Planar sliding travelling along a surface not totally planar	Mohr-Coulomb frictional strength Constant frictional coefficient Constant thermal expansion coefficient Thermal decomposition of Dolomite which involve increments in porosity	The Heart Mountain landslide in Canada.	Simulation of the long runout features of the simulated landslides

			Non constant permeability		
Cecinato et al. (2011) Cecinato and Zervos (2012)	As in V&F(1982) Numerical analysis Heat advective term negligible	Planar and slip circle	Thermoplastic Modified Cam clay Strain, strain rate and temperature softening of the critical state parameter function of the friction angle at critical states Thermal expansion coefficient of the soil skeleton including thermoelastic expansion and thermoplastic collapse	Vaiont in Cecinato et al. (2011) Jiufenghershan landslide (Taiwan) in Cecinato and Zervos (2012)	Evaluation the effect of the thermal, strain and strain rate softening and the pressurization mechanism in Cecinato et al. (2011) Parametric analysis in Cecinato and Zervos (2012)
He et al. (2015)	As in V&F(1982) Numerical analysis Advective term and heat conduction negligible Depth-average integration model	Planar	Mohr-Coulomb frictional strength Constant frictional coefficient Constant thermal expansion coefficient	Synthetic case	A depth-averaged model coupled with a thermo-poro-elastic approach in the shear zone

Table 2. Material properties for water and solid particles

Parameter	*Symbol*	*Value*	*Unit*
	Water		
Density	ρ_w	1,000	kg/m^3
Coefficient of compressibility	α_w	5×10^{-10}	1/Pa
Thermal expansion coefficient	β_w	3.42×10^{-4}	1/ºC
Specific heat	c_w	4.186×10^{3}	J/kg·ºC
Conductivity	Γ	0.580	J/m·s·ºC
	Solid particles		
Density	ρ_s	2,700	kg/m^3
Thermal expansion coefficient	β_s	3×10^{-5}	1/ºC
Specific heat	c_s	8.372×10^{-2}	J/kg·ºC
Conductivity	Γ	0.375	J/m·s·ºC
	Soil		
Porosity	*n*	0.2	-

Table 3. Typical ranges permeability, coefficient of compressibility and band thickness

Parameter	*Symbol*	*Range of value*	*Unit*
Permeability	*k*	$10^{-13}-10^{-5}$	m/s
Coefficient of compressibility	m_v	$10^{-10}-10^{-8}$	1/Pa

Shear band thickness	2*e*	0.001-0.05	M